

# Quantization Phenomena of critical Hamiltonians in 2D systems

S. C. Chen<sup>1</sup>, J. Y. Wu<sup>2</sup>, C. Y. Lin<sup>1</sup>, and M. F. Lin<sup>1</sup>

<sup>1</sup>Department of Physics, National Cheng Kung University, Tainan, Taiwan 701

<sup>2</sup>Center of General Studies, National Kaohsiung Marine University, Kaohsiung 811, Taiwan

This review work addresses the recent advances in solving more comprehensive Hamiltonians. The generalized tight-binding model is developed to investigate the feature-rich quantization phenomena in emergent 2D materials. The multi-orbital bondings, the spin-orbital interactions, the various geometric structures, and the external fields are taken into consideration simultaneously. Specifically, the IV-group layered systems, black phosphorus and MoS<sub>2</sub> exhibit the unique magnetic quantization. This is clearly indicated in three kinds of Landau levels (LLs), the orbital-, spin- and valley-dependent LL groups, the abnormal LL energy spectra, and the splitting, crossing and anticrossing behaviors. A detailed comparison with the effective-mass model is made. Some theoretical predictions have been confirmed by the experimental measurements.

## I. INTRODUCTION

How to solve the Hamiltonian is one of the basic topics in physics science. It is very interesting to comprehend the diverse quantization phenomena due to the various Hamiltonians in condensed-matter systems, especially for the feature-rich magnetic quantization. Such Hamiltonians possess the complex effects coming from the multi-orbital bondings, the spin-orbital coupling (SOC), the magnetic field ( $\mathbf{B} = B_z \hat{z}$ ), the electric field ( $\mathbf{E} = E_z \hat{z}$ ), the interlayer hopping integrals, the number of layers, the stacking configurations, the curved surfaces, the hybridized structures, and the distinct dimensionalities. The generalized tight-binding model is developed to include the critical interactions simultaneously. The quantized energy spectra and wave functions can be computed very efficiently by the exact diagonalization method even for a rather large Hamiltonian with complex matrix elements. This model has been used to make systematic studies on the three-dimensional (3D) graphites [1–6], 2D graphenes [7–12], and 1D graphene nanoribbons [13–15]. It is further extended to the mainstream layered materials, e.g., other group-IV systems [16–19], and MoS<sub>2</sub> [20–22]. Moreover, the generalized tight-binding model can directly combine with the single- and many-particle theories to study the other essential physical properties, such as, magneto-optical properties [15, 23–28] and Coulomb excitations [17, 18, 29–31]

On the other hand, the perturbation method is frequently used to investigate the low-energy electronic states and magnetic quantization. It is very suitable for the condensed-matter systems with monotonous band structures. For example, the effective-mass model can deal with the magnetic quantization in monolayer graphene [32–35], AA- and AB-stacked few-layer graphenes [36–41], monolayer silicene and germanene [42], MoS<sub>2</sub> [43], and black phosphorus [44]. This model will become too complex or cumbersome to magnetically

quantize the multi-valley and/or multi-orbital electronic states, such as, the magnetic quantization for the oscillatory energy bands in ABC- and AAB-stacked graphenes [9, 12], the seriously distorted Dirac-cone structure in sliding bilayer graphenes [7], the three constant-energy loops due to the significant  $sp^3$  bondings in monolayer tinene [16], and the mixed energy bands in hybridized carbon systems [45–49]. Furthermore, it is very difficult to resolve the complex quantization phenomena in the presence of the non-uniform or the composite external fields [50–53].

The layered condensed-matter systems have stirred a lot of experimental [54–59] and theoretical studies [7, 9–12, 32, 34, 36, 178], mainly owing to the nano-scaled thickness and the specific symmetries. They are ideal 2D materials for studying the novel physical, chemical and material phenomena. Furthermore, such systems have shown high potentials for future technological applications, e.g., nano-electronics [60–67], optoelectronics [68–79] and energy storage [80–93]. Few-layer graphenes have been successfully synthesized by the distinct experimental methods, such as, mechanical exfoliation [94–104], electrostatic manipulation of scanning tunneling microscopy (STM) [105–109], and chemical vapor deposition [110–129]. Four kinds of typical stacking configurations, AAA [114, 128], ABA [113, 116, 119], ABC [111, 112] and AAB [113, 129], are clearly identified in the experimental measurements. It should be noticed that the STM tip can generate the continuous changes in the stacking configuration, e.g., the configuration transformation among the ABA, ABC and AAB stackings [107].

The essential electronic properties of planar graphenes are dominated by the  $2p_z$ -orbital hybridization, the hexagonal honeycomb symmetry, the stacking configuration and the number of layers. The main features of low-lying energy bands are further reflected in the

rich magnetic quantization. The tri-layer AAA, ABA, ABC and AAB stackings, respectively, have the unusual energy dispersions: (1) the linearly intersecting bands (the almost isotropic Dirac-cone structures) [11, 36], (2) the parabolic bands and the linear bands [10], (3) the weakly dispersive bands, the sombrero-shaped bands, and the linear bands [9]; (4) the oscillatory bands, the sombrero-shaped bands, and the parabolic bands [12]. Such stacking systems exhibit the novel Landau levels (LLs), in which the rich magneto-electronic properties include the diverse  $B_z$ -dependent energy spectra, the asymmetric energy spectra about the Fermi level ( $E_F$ ), the crossing and/or anti-crossing behaviors, the main and side modes, and the configuration- and  $E_z$ -created splitting states. Specifically, the configuration transformation between AA and AB stackings will induce the thorough destruction of the Dirac-cone structures. The three kinds of LLs, the well-behaved, perturbed and undefined LLs, are predicted to reveal in the changes from the linear to the parabolic bands

Few-layer germanene and silicene can be synthesized on distinct substrate surfaces, e.g., Si on Ag(111), Ir(111) & ZrB<sub>2</sub> surfaces [130–134]; Ge on Pt(111), Au(111) & Al(111) surfaces [135–137]. Germanene and silicene possess the buckled structures with a mixed  $sp^2$ - $sp^3$  bonding rather than a  $sp^2$  bonding, since the relatively weak chemical bonding between the larger atoms cannot maintain a planar structure (Fig. 1(b)). These two systems have the significant SOC's much stronger than that in graphene. The SOC's can separate the Dirac-cone structures built from the dominating  $3p_z$  or  $4p_z$  orbitals; that is, the intrinsic systems are narrow-gap semiconductors ( $E_g \sim 45$  meV for Ge &  $E_g \sim 5$  meV for Si) [138, 139]. Furthermore, the application of a uniform perpendicular electric field leads to the modulation of energy gap and the splitting of spin-related configurations [42, 140, 141]. The



magneto-electronic properties are greatly enriched by SOC and  $E_z$ , including the modified  $B_z$ -dependent energy spectra, the spin-up- and spin-down-dominated states, and the  $E_z$ -generated crossing and anti-crossing behaviors.

Monolayer tinene is successfully fabricated on a substrate of bismuth telluride [142], while monolayer Pb system is absent in the experimental measurements up to now. The theoretical studies show that the single-layer Sn and Pb systems have rather strong  $sp^3$  bondings and SOC's [138, 143]. Apparently, the complex chemical bondings from  $(s, p_x, p_y, p_z)$  orbitals need to be included in the low-energy model calculations. However, the low-lying electronic structures of graphene, silicene and germanene are mainly determined by the  $p_z$  orbitals. The very pronounced mixing effects of multi-orbital bondings and SOC's can create the  $p_z$ - and  $(p_x, p_y)$ -dominated energy bands near  $E_F$ , indicating the existence of the multi-constant-energy loops. There exist two groups of low-lying LLs, with the different orbital components, spin configurations, localization centers, state degeneracy, and  $B_z$ - and  $E_z$ -dependencies. Specially, the LL splitting and anti-crossing behaviors strongly depend on the type of orbitals and the external fields. The competitive or cooperative relations among the orbital hybridizations, SOC,  $\mathbf{B}$  and  $\mathbf{E}$  are worthy of detailed investigations.

The group-V phosphorus possesses several allotropes in which black phosphorus (BP) is the most stable phase under normal experimental conditions [144]. Few-layer phosphorene is successfully obtained using the mechanical cleavage approach [145, 146], liquid exfoliation [147–149], and mineralizer-assisted short-way transport reaction [150–152]. Specially, the experimental measurements show that the BP-based field effect transistor has an on/off ratio of 105 and a carrier mobility at room temperature as high as  $103 \text{ cm}^2/\text{Vs}$ . BP is expected to play an important role in the next-generation electronic devices [146, 153]. Phos-

phorene exhibits a puckered structure related to the  $sp^3$  hybridization of  $(3s, 3p_x, 3p_y, 3p_z)$  orbitals. The deformed hexagonal lattice of monolayer BP has four atoms [154], while the group-IV honeycomb lattice includes two atoms. The low-lying energy bands are highly anisotropic, e.g., the linear and parabolic dispersions near  $E_F$ , respectively, along the  $\hat{k}_x$  and  $\hat{k}_y$  directions. The anisotropic behaviors are further reflected in other physical properties, as verified by recent measurements on optical spectra and transport properties [153, 155]. BP has a middle energy gap of  $\sim 1.5 - 2$  eV at the  $\Gamma$  point, being quite different from the narrow or zero gaps of group-IV systems. The low-lying energy dispersions, which are dominated by  $3p_z$  orbitals, can be described by a four-band model with the complicated multi-hopping integrals [154]. The low-energy electronic structure is easily tuned by a perpendicular electric field, e.g., the monotonic increase of  $E_g$  with  $E_z$  in monolayer BP, and the transition from a semiconducting to a gapless system in bilayer BP. [156, 157]. In sharp contrast with the group-IV monolayer systems, monolayer phosphorene presents the unique LLs, with the asymmetric energy spectrum about  $E_F$ , the reduced state degeneracy, and the spin-independent configuration. The important differences mainly come from the geometric structure, the orbital hybridization, and the SOC. The magnetic quantization is greatly diversified by the number of layers.

The transition metal dichalcogenide monolayers can be produced by the micromechanical cleavage [158–161], liquid-phase exfoliation [162, 163] and chemical vapor deposition [164–167]. Due to the unusual electronic and optical properties, various technological applications have been proposed for these materials, such as, electronic [54, 168–171] and optoelectric [171–173] devices. The high potentials in the field-effect transistors are supported by the room-temperature carrier mobility over  $200 \text{ cm}^2/\text{Vs}$  and the high on/off ratio

of  $\sim 10^8$  [54]. Furthermore, the experimental measurements show that they have a direct band gap in the visible frequency range [161, 174, 175] and the valley-dependent optical selection rules [172, 176]. The stronger SOC and the inversion symmetry breaking lead to the spin- and valley-dependent electronic states [172]. The MoS<sub>2</sub>-related systems are very suitable for investigating the spintronics and valleytronics. Specifically, the single-layer MoS<sub>2</sub> is composed of staggered honeycomb-like lattice structures in which a single layer of Mo atoms is sandwiched by two sulfur layers. This semiconducting system has a direct energy gap of  $\sim 1.59$  eV [22]. The low-lying electronic states near three valleys centered at the  $(K, K')$  and  $\Gamma$  points are dominated by the  $(4d_{z^2}, 4d_{xy}, 4d_{x^2-y^2})$  orbitals of Mo atoms. The SOC can effectively destroy the spin degeneracy of energy bands, especially for the valence one contributed by the  $4d_{xy}$  and  $4d_{x^2-y^2}$  orbitals. The quantized LLs are characterized by the dominating orbitals and spin configurations, being enriched by the constant-energy loops in three valleys. The degeneracy of the  $K$  and  $K'$  valleys is further lifted by  $\mathbf{B}$ , owing to the cooperation of the site-energy difference and the magnetic quantization [22].

## II. GRAPHENE

The Hamiltonian of the layered graphene, which is built from the  $2p_z$ -orbital tight-binding functions in a unit cell, is expressed as

$$H = \sum_{\langle ij \rangle \langle ll' \rangle} -\gamma_{ij}^{ll'} C_{il}^+ C_{jl'}, \quad (1)$$

where  $\gamma_{ij}^{ll'}$  is the intralayer or interlayer hopping integral,  $i$  the lattice site, and  $l$  the layer index.  $C_{il}^+$  ( $C_{jl'}$ ) can create (annihilate) an electron at the  $i$ -th ( $j$ -th) site of the  $l$ -th ( $l'$ -th) layer. A hexagonal unit cell has  $2N$  carbon atoms for a  $N$ -layer graphene. Under a uniform perpendicular magnetic field, there are  $4NR_B$  carbon atoms in an enlarged rectangular unit cell (Fig. 1(a)), since the vector potential ( $\mathbf{A} = [0, B_z x, 0]$ ) can induce a

periodical Peierls phase.  $R_B$  is the ratio between flux quantum ( $\phi_0=hc/e$ ) and magnetic flux through a hexagon ( $\phi=3\sqrt{3}b^2B_z/2$ ;  $b$  the C-C bond length), e.g.,  $R_B=2\times 10^3$  at  $B_z=40$  T. The quantized LLs are highly degenerate in the reduced first Brillouin zone with an area  $4\pi^2/3\sqrt{3}b^2R_B$ . The ( $k_x=0, k_y=0$ ) Hamiltonian, with the real matrix elements, is sufficient in calculating energy spectra and wavefunctions. Each LL wavefunction is the superposition of the  $4NR_B$  tight-binding functions:

$$|\Psi_{\mathbf{k}}\rangle = \sum_{i,l} A_i^l |A_{i\mathbf{k}}^l\rangle + B_i^l |B_{i\mathbf{k}}^l\rangle. \quad (2)$$

$A_i^l$  and  $B_i^l$  are the probability amplitudes of the subenvelope functions in the two equivalent sublattices.

The hexagonal symmetry in monolayer graphene can create the low-lying isotropic Dirac-cone structure and thus the well-behaved LLs with the specific dependence on quantum number ( $n^{c,v}$ ) and field strength. As to each ( $k_x, k_y$ ) state, all the LLs have eight-fold degeneracy. This comes from the equivalent  $K$  and  $K'$  valley, the symmetry of  $\pm\mathbf{B}$  and the spin degree of freedom. At ( $k_x=0, k_y=0$ ), the state probabilities of the degenerate LLs are localized at the 1/6, 2/6, 4/6 and 5/6 positions of the enlarged unit cell. The (2/6, 5/6) and (1/6, 4/6) states, respectively, correspond to the magnetic quantization from the  $K$  and  $K'$  valleys [7]. The 2/6 localized LL wavefunctions, as shown in Fig. 2, have the normal probability distributions, being identical to those of a harmonic oscillator. Quantum number of each LL is characterized by the number of zero points in the dominating B sublattice. The  $n^{c,v}=0$  LLs only come from the B sublattice. In general, the  $n^{c,v}$  LL wavefunctions in the B sublattice are proportional to the  $(n^{c,v}+1)$  LL wavefunction in the A sublattice, directly reflecting the honeycomb symmetry. The same features are revealed in the 1/6 case under the interchange of two sublattices. Specifically, the low energy spectrum is characterized

by  $E^{c,v} = \pm v_F \sqrt{2\hbar e n^{c,v} B_z / c}$  ( $v_F$  the Fermi velocity), consistent with that obtained from the effective-mass model [32, 34]. The square-root dependence is suitable at  $|E^{c,v}| < 1$  eV, since the linear bands gradually change into the parabolic bands in the increment of state energy. In addition, the high-energy LL spectrum can also be obtained by the generalized tight-binding model [8, 11]. Specifically, the dispersionless feature of 2D LLs is dramatically changed by the distinct dimensions, e.g., the 1D quasi-LLs and the 3D Landau subbands (discussed in conclusion).

The main features of LLs, energy spectra, spatial distribution modes and state degeneracy, are dramatically changed by the number of layers, the stacking configurations, and the perpendicular electric field. The LLs in the layered graphenes might exhibit the asymmetric energy spectra about the Fermi level, the non-square-root or non-monotonous dependence on  $n^{c,v}$  and  $B_z$ , and the crossing or anti-crossing behaviors, mainly owing to the critical interlayer hopping integrals (Fig. 3(a)). Such interactions can induce three kinds of LLs with the distinct distribution modes: (1) the well-behaved LLs in a single mode, (2) the perturbed LLs with a main mode and side modes, and (3) the undefined LLs composed of many comparable modes (Fig. 4). The LL degeneracy will be reduced to half, when the  $z \rightarrow -z$  inversion symmetry is destroyed by the perpendicular electric field (Fig. 12(a)) or the specific stacking configuration. For example, the trilayer AAB-stacked graphene has an obvious splitting LL spectrum with observable spacings about 10 meV [12].

The ABC-stacked tetralayer graphene and the sliding bilayer graphene are chosen to see the geometry-enriched magnetic quantization. The former has four groups of LLs, in which the quantum numbers of the first, second, third and fourth groups (black, red, blue and green curves) are, respectively, obtained from the dominant ( $B^1$ ,  $B^3$ ,  $B^2$ ,  $B^4$ ) sublattices

at the 2/6 center. Apparently, the valence and the conduction LLs are asymmetric about  $E_F$  (Fig. 4). The LL energy spectrum exhibits the diverse  $B_z$ -dependences, indicating the sensitive changes of energy bands with wave vectors (Fig. 3(b)). In general, the first group of LLs has the monotonous dependence, i.e., their energies grow with the increasing  $B_z$ . However, the four LLs nearest to  $E_F$ , which mainly arise from the weakly dispersive energy bands dominated by the surface states (black curves), have distribution widths smaller than 8 meV even at rather high  $B_z$  (Fig. 4(c)). The LLs, which are localized at two outmost graphene layers, are absent in the AA-, AB- and AAB-stacked graphenes [9, 12].

Specifically, the second group of LLs exhibit the abnormal  $n_2^{c,v}$  sequence and the unusual energy spectrum, as seen in the conduction and valence states. At rather small  $B_z$ , all the LLs have the reverse ordering of  $E^c(n_2^c) < E^c(n_2^c - 1)$ . They are initiated at a specific energy corresponding to the cusp  $K$  point of the sombrero-shaped energy band (red curves). This clearly illustrates that LLs are quantized from the electronic states enclosed by the inner constant-energy loops. With the increase of  $B_z$ , the higher- $n_2^c$  LLs come to exist in the normal ordering, since they arise from the outer constant-energy loops related to parabolic dispersions. The completely normal ordering of  $E^c(n_2^c) < E^c(n_2^c + 1)$  is revealed only at  $B_z > 100$  T, directly reflecting the fact that the electronic states under the cusp-shaped energy dispersions are only quantized into the  $n_2^c = 0$  LLs. The ordering of LLs is mainly determined by the competitive relation between the area covered by the cusp-shaped energy dispersions and the  $B_z$ -enhanced state degeneracy [details in Ref. [11]].

The novel intragroup anticrossings appear frequently in the non-monotonous LL spectrum, as seen in the range of  $0.29 \text{ eV} < E^c(n_2^c) < 0.36 \text{ eV}$ . In addition to a main mode, the specific interlayer hopping integrals,  $(\beta_3, \beta_2, \beta_5)$  (Fig. 3(a)), cause the  $n_2^c$  LLs to possess

certain side modes with the zero points of  $n_2^c \pm 3I$  ( $I$  an integer) [9, 11, 177, 178]. The lower- $n_2^c$  perturbed LLs exhibit the distorted spatial distributions (Figs. 5(j)-5(k)); that is, they significantly deviate from the monolayer-like single modes (Fig. 2). For example, with the increase of  $B_z$ , the wave functions are drastically changed during the anticrossing of the  $n_2^c=0$  and 3 LLs, as shown in Fig. 5. When the side mode, with three zero points in the  $n_2^c=0$  LL (or without zero point in the  $n_2^c=3$  LL), becomes comparable with their main mode, the same oscillation modes in these two LLs can prevent the direct crossing. Apparently, the intragroup LL anticrossings are derived from the magnetic quantization of the non-monotonous energy bands, e.g., the existence in the AAB-stacked graphenes and the absence in the AA- and AB-stacked graphenes [12]. It should be noticed that the LL anticrossings are also presented between any two distinct groups at sufficiently high  $B_z$  and  $|E^{c,v}|$  [9], i.e., there exist the intergroup LL anticrossings. Except for the regimes of these anticrossings, the third and the fourth groups of energy spectra have the normally continuous  $B_z$ -dependence (blue and green curves in Fig. 4). The similar anticrossing behaviors are shown in the AB and AAB stackings, but not in the AA stacking only with the single-mode LLs.

In addition to the well-behaved and the perturbed LLs, the undefiled LLs can be created during the transformation of stacking configuration. Specially, the stacking configuration could be changed by the electrostatic-manipulation STM [106, 107]. When the configuration of bilayer graphene is transformed from the AA to AB stacking by the shift along the armchair direction (Fig. 6(a)), two vertical Dirac cones gradually change into two pairs of parabolic bands. Each Dirac-cone structure is seriously distorted and thoroughly separated at the critical shift of  $\sim 6b/8$  (Fig. 6(b)). It is impossible to get the low-lying energy bands

from the  $K$ -point expansion, and so does the LL quantization using the effective-mass model. The  $\delta=6b/8$  stacking exhibits the eight-fold degenerate LLs, being the same with monolayer graphene. However, this bilayer system has a lot of undefined LLs, as indicated in the unusual  $B_z$ -dependent energy spectrum at  $|E^{c,v}| > 0.3$  eV (Fig. 6(c)). Each LL in the second group is composed of various zero points, and the irregular spatial distribution is very sensitive to the change in field strength. As a result, it displays the significant anticrossings with all the LLs in the first group.

### III. SILICENE, GERMANENE & TINENE

For the IV-group inorganic layered systems, the  $sp^3$  orbital bondings and the SOC's are included in the critical Hamiltonians. In the bases of  $\{|p_z^A\rangle, |p_x^A\rangle, |p_y^A\rangle, |s^A\rangle, |p_z^B\rangle, |p_x^B\rangle, |p_y^B\rangle, |s^B\rangle\} \otimes \{\uparrow, \downarrow\}$ , the nearest-neighbor Hamiltonian is expressed as

$$H = \sum_{\langle i \rangle, o, m} E_o C_{iom}^+ C_{iom} + \sum_{\langle i, j \rangle, o, o', m} \gamma_{oo'}^{\mathbf{R}_{ij}} C_{iom}^+ C_{jo'm} + \sum_{\langle i \rangle, p_\alpha, p_\beta, m, m'} \frac{\lambda_{\text{SOC}}}{2} C_{ip_\alpha m}^+ C_{ip_\beta m'} (-i\epsilon_{\alpha\beta\gamma} \sigma_{mm'}^\gamma), \quad (3)$$

where  $i(j)$ ,  $o(o')$ , and  $m(m')$  stand for the lattice site, atomic orbital, and spin, respectively. The first and second terms are, respectively, the site energy ( $E_o$ ) and the nearest-neighbor hopping integral ( $\gamma_{oo'}^{\mathbf{R}_{ij}}$ ). The latter is determined by the type of atomic orbitals, the translation vector  $\mathbf{R}_{ij}$ , and the angle  $\theta$  between  $\mathbf{R}_{ij}$  and  $\hat{z}$  (Fig. 1(c)). The details of interaction energies are given in Ref. [138]. The last term represents the SOC on the same atom where  $\alpha, \beta$  and  $\gamma$ , respectively, denote the  $x, y$  and  $z$  components, and  $\sigma$  is the Pauli spin matrix. The SOC strength is, respectively, predicted to be  $\lambda_{\text{SOC}}=0.034, 0.196; 0.8$  eV's for (Si, Ge, Sn) [138]. The SOC between  $|p_x\rangle$  and  $|p_y\rangle$  can create the splitting of states with opposite spin configurations, while that between  $|p_z\rangle$  and  $|p_x\rangle$  ( $|p_y\rangle$ ) leads to the splitting of states and an interchange of spin configurations. Specially, the magnetic Hamiltonian of



monolayer system is a  $32R_B \times 32R_B$  Hermitian matrix with complex elements.

The SOC, buckled structure and orbital hybridizations in IV-group can induce the feature-rich energy bands and diversify the quantized LLs. Germanene and silicene have the similar band structures, in which the low-lying electronic states mainly come from the  $4p_z$  and  $3p_z$  orbitals, respectively. A small direct energy gap, which corresponds to the slightly separated Dirac points, is dependent on the strength of SOC.  $E_g$  is, respectively, 45 meV and 5 meV for Ge and Si systems (inset in Fig. 7(a)). The first pair of valence and conduction bands have the doubly degenerate states associated with the spin-down- and spin-up-dominated equivalent configurations. It is sufficient to only discuss one of both configurations, as shown in Figs. 7(b) and 7(c) for germanene. Near the  $K$  ( $K'$ ) point, the valence states are mainly determined by the  $|4p_z^B; \downarrow\rangle$  and  $|4p_z^A; \downarrow\rangle$  ( $|4p_z^B; \uparrow\rangle$  and  $|4p_z^A; \uparrow\rangle$ ). Their contributions are very sensitive to the changes of wave vectors along  $K \rightarrow M$  ( $K' \rightarrow \Gamma$ ) (solid curves in Fig. 7(b)). The similar behaviors are revealed in the conduction states under the interchange of the A and B sublattices (Fig. 7(c)). In addition, the  $(4p_x, 4p_y, 4s)$  orbitals can make important contributions to the middle-energy states close to the  $\Gamma$  point.

The quantized LLs in monolayer germanene (silicene) are characterized by the subenvelope functions on the A and B sublattices with  $sp^3$  orbitals and two spin configurations. All the low-lying LLs in monolayer germanene (silicene) belong to the well-behaved modes. They are eight-fold degenerate for each  $(k_x, k_y)$  state except the four-fold degenerate LLs of  $n^{c,v}=0$ . As to each localization center, there are two subgroups characterized by the up- and down-dominated configurations, as indicated in Fig. 8(a)-8(d) for the 2/6 states. The first and the second subgroups, respectively, have the  $n^c=0$  conduction LL and the  $n^v=0$  valence LL at  $E^c=23$  meV and  $E^v=-20$  meV. The former and the latter are caused by the

spin-up and spin-down configurations in the dominating B sublattice, respectively. The other  $n^{c,v} \neq 0$  LLs in these two subgroups are doubly degenerate, and their wave functions are identical under the interchanges of spins and weights of A and B sublattices. There exist certain important differences between germanene and graphene. Germanene exhibits the significantly splitting  $n^{c,v}=0$  LLs with the partial contributions from the A sublattice. The weight ratio between the A and B sublattices are quite different for the valence and conduction LLs. In addition to the dominating  $4p_z$  orbitals, the contributions due to the ( $4p_x, 4p_y, 4s$ ) orbitals are gradually enhanced as  $|E^{c,v}|$  grows. However, the opposite is true for graphene (Fig. 2).

A perpendicular electric field applied to buckled systems can split energy bands and even induce the anti-crossing LL spectra. The destruction of the  $z=0$  mirror symmetry causes one Dirac cone to become two splitting structures, when the gate voltage between two sublattices ( $V_z$ ) grows from zero. The lower cone structure approaches to the Fermi level, and energy gap is vanishing at a critical  $V_z$  where the linearly gapless Dirac-cone structure is recovered (the inset of Fig. 9(a)). The dependence of  $E_g$  on  $V_z$  is in the cusp form. Another cone structure is always away from  $E_F$ . The  $V_z$ -dependent cone structures are quantized into the unusual LL energy spectra (Fig. 9(a)). The K-valley-dependent (or the  $K'$ -valley-dependent) LLs are split according to the magnetic quantization of the lower and higher Dirac structures. The  $n^{c,v} > 0$  and  $n^{c,v}=0$  LLs, respectively, have the four-fold and double degeneracy. The splitting LL energy spectrum, which corresponds to the lower Dirac cone, exhibits the non-monotonous  $V_z$ -dependence. As a result, the intra-group LL anticrossings occur frequently in the plentiful LL energy spectrum. In addition, the  $V_z$ -induced LL splittings and anticrossings are also presented in the layered graphenes except

for the AA-stacked systems [179].

The cooperation of the electric field and spin-orbital coupling can create the significant probability transfer between the spin-up and spin-down configurations and thus the frequent intra-group LL anticrossings. For example, the  $n_K^v=2$  and  $n_K^v=3$  LLs exhibit the dramatic changes in the spatial distributions within the critical range of  $150 \text{ meV} < V_z < 350 \text{ meV}$  (green and purple triangles in Fig. 9(b)). At small  $V_z$ 's, these two  $4p_z$ -dominated LLs have the same quantum modes on the  $(A_\uparrow, B_\uparrow)$  and  $(A_\downarrow, B_\downarrow)$  sublattices (Fig. 9(c) and (d)). However, the weight of distinct spin configurations is very large and small for the former and the latter, respectively. With the variation of  $V_z$ , the electric field can induce the probability transfer between  $A_\uparrow$  and  $B_\uparrow$  ( $A_\downarrow$  and  $B_\downarrow$ ) sublattices. Furthermore, the intra-atomic SOC of  $4p_z$  and  $(4p_x, 4p_y)$  orbitals leads to the significant distribution change on  $A_\uparrow$  and  $A_\downarrow$  ( $B_\uparrow$  and  $B_\downarrow$ ) sublattices. This means that the latter two orbitals play an important role in the anti-crossing behaviors, even if they have small weights. The comparable probability distributions on the spin-related sublattices are responsible for the anti-crossings of the  $n_K^v$  and  $n_K^v+1$  LLs (the  $n_K^c$  and  $n_K^c+1$  LLs). In addition, the direct crossing from the  $n_{K'}^v$  and  $n_{K'}^v+1$  LLs (the  $n_{K'}^c$  and  $n_{K'}^c+1$  LLs) occurs simultaneously.

Tinene has more low-lying energy bands and diverse LLs, compared with germanene and silicene. A pair of slightly distorted Dirac cones appears near the K point, and there are parabolic energy bands initiated at the  $\Gamma$  point (Fig. 10(a)). The latter, which mainly originate from the  $(5p_x, 5p_y)$  orbitals, are attributed to the stronger  $sp^3$  bonding. State degeneracy at the  $\Gamma$  point is further destroyed by the critical SOC between  $5p_x$  and  $5p_y$  orbitals so that one of the parabolic bands is very close to the Fermi level. The Dirac-cone structure is quantized into the first group of LLs (the black curves Fig. 11(a)), in which

the main features are similar to those in germanene (Figs. 8(b) and 8(d)), such as, the  $p_z$ -orbital dominance, localization centers, state degeneracy, spin configurations, quantum modes on the A and B sublattices, and  $B_z$ -dependence of LL energy spectrum. However, the first group is in sharp contrast to the second group. Both  $5p_x$  and  $5p_y$  orbitals dominate the second group of LLs and make the almost same contributions (red and green curves in Fig. 10 (e)). Such LLs only have two equivalent centers of 1 and  $1/2$ , and they are doubly degenerate (Fig. 10(d)). For each center, the splitting LLs are characterized by the up- and down-dominated configurations ( $n_{\Gamma,\uparrow}^{c,v}$  &  $n_{\Gamma,\downarrow}^{c,v}$ ), being attributed to the significant effect of SOC. The spin-split LL energy spacing is observable, especially for the larger spacing in the conduction LLs. This spacing grows with the enhanced weight ratio of two spin configurations on the same sublattice. Specifically, the A and B sublattices present the same quantum modes, since the nearest-neighbor hopping integrals near the  $\Gamma$  point are roughly proportional to the square of wave vector. However, the hexagonal symmetry can generate the linear  $k$ -dependence in these atomic interactions near the  $K$  point. As to the first group, this accounts for the mode difference of one between the A and B sublattices.

Tinene exhibits the rich  $B_z$ -dependent energy spectrum and density of states (DOS). Two group of LLs have the well-behaved modes, as indicated from the absence of anti-crossings and the existence of intergroup crossings (Fig. 11(a)). The LL state energies grow with the increase of field strength except the almost unchanged  $n_K^{c,v}=0$  ones. As to the first and the second groups, the  $B_z$ -dependence is presented in the square-root and the linear forms, respectively (black and blue curves). This directly reflects the magnetic quantization from the linear and the parabolic energy dispersions. The spin-split energy spacings in the second group gradually become large, since the higher field strength creates more localized

LL wave functions and enhances the spin-up or spin-down dominance. That is to say, the splitting energies are enlarged by the stronger effects of SOC. The main differences between two groups of energy spectra are further presented in DOS (Fig. 11(b)). A lot of strong peaks appear in the delta-function-like symmetric structure, in which their heights are proportional to state degeneracy. The single- and double-peak structure originate from the first and the second groups of LLs; furthermore, the former have the larger peak spacings. The main features of DOS peaks, structure, height, number and energy, could be verified from the experimental measurements using scanning tunneling spectroscopy (STS) [180–184].

The  $V_z$ -dependent LL energy spectra are quite different among the IV-group layered systems. The splitting LLs cannot survive only in the AA-stacked graphenes, since the mirror symmetry is preserved even in the composite magnetic and electric fields [179]. For monolayer silicene, the splitting energy spacings are very small, and the LL anti-crossings and crossings are absent (Fig. 12(a)). The weak SOC and the large  $v_F$  (the strong energy dispersion) are responsible for the monotonous  $V_z$ -dependence. However, monolayer germanene and tinene frequently exhibit intragroup anti-crossings and crossings (Figs. 9(a) and 12(b)), in which two anti-crossing LLs have quantum number difference of  $\Delta n=1$ . Specifically, the latter have the intergroup crossings between the  $5p_z$ - and  $(5p_x, 5p_y)$ -dominated LLs. The  $V_z$ -induced intragroup anti-crossings are also observed in the non-AA-stacked graphenes, while they arise from two LLs with  $\Delta n=3I$  [9, 11, 177, 178]. In addition to  $V_z$ ,  $\Delta n=1$  and  $3I$  are, respectively, determined by the significant SOC's and certain interlayer hopping integrals.

#### IV. BLACK PHOSPHORUS

Monolayer phosphorene, with a puckered honeycomb structure, has a rectangular unit cell. There are four phosphorus atoms, in which two ones are situated at lower and upper subplanes (Fig. 13). The low-energy band structure is characterized by the  $3p_z$ -orbital hybridizations. The few-layer Hamiltonian is expressed as

$$H = \sum_{\langle ij \rangle \langle ll' \rangle} -t_{ij}^{ll'} C_{il}^+ C_{jl'},$$

where  $t_{ij}^{ll'}$  represents the five intralayer (Fig. 13(a)) and four interlayer hopping integrals (Fig. 13(b); details in Ref. [154]). For monolayer system, the magnetic Hamiltonian is a  $4R_B \times 4R_B$  Hermitian matrix.

The energy bands are greatly enriched by the complicated multi-hopping integrals. Monolayer phosphorene has a direct gap of  $\sim 1.6$  eV near the  $\Gamma$  point (Fig. 14(a)), being in sharp contrast with that dominated by the  $K$  point in the group-IV systems. The first pair of energy bands nearest to  $E_F$  is, respectively, linear and parabolic along  $\Gamma X$  and  $\Gamma Y$  directions. The valence (conduction) band is due to the linearly anti-symmetric (symmetric) superposition of the tight-binding functions on the upper and lower subplanes. As to bilayer phosphorene, two pairs of low-lying bands have parabolic dispersions, as shown in Fig. 14(b). The first and second pairs, respectively, correspond to the in-phase and out-of-phase combinations of two layers.

The quantized LLs in phosphorene are characterized by the subenvelope functions on the different subplanes and sublayers. They are localized at the  $1/2$  and  $2/2$  positions of the enlarged unit cell, corresponding to the magnetic quantization at the  $\Gamma$  point. The well-behaved spatial distributions, as shown in Fig. 15(b), are similar to those of monolayer graphene. The  $3p_z$ -orbit quantization, with spin degree, is four-fold degenerate for each  $(k_x, k_y)$  state. This is in sharp contrast to the eight-fold degeneracy in the group-IV

systems, or the double degeneracy of the spin- and valley-dependent LLs in MoS<sub>2</sub>. The LL degeneracy depends on the number of equivalent valleys and the existence of inversion symmetry ( $z \rightarrow -z$  and  $x \rightarrow -x$ ). There are two groups of valence and conduction LLs in bilayer phosphorene (the black and red lines in Fig. 15(a)). Both of them differ from each other in the initial energies and level spacings. The first and second groups, respectively, correspond to the in-phase and out-of-phase subenvelope functions on sublayers (Fig. 15(c)).

The highly asymmetric energy dispersion leads to the special dependence of LL energies on  $(n^{c,v}, B_z)$ , as clearly indicated in Fig. 16. In monolayer and bilayer phosphorene, the low-lying LL energies cannot be described by a simple relation with  $n^{c,v} B_z$ , especially for the higher energy and field strength. This is different from the square-root dependence in monolayer group-IV systems (Fig. 11) [8], and the linear dependence in AB-stacked graphene [9, 11] and MoS<sub>2</sub> (Fig. 19). In general, the LL energies grow with the increment of  $B_z$  monotonously. Only the intergroup LL crossings are revealed in bilayer system (Fig. 16(b)). However, the intragroup and the intergroup anticrossings are absent, since all the well-behaved LLs are quantized from the monotonous band structure in the energy-wave-vector space (Fig. 14).

## V. MoS<sub>2</sub>

A MoS<sub>2</sub> monolayer consists of three centered honeycomb structures, in which the middle Mo-atom lattice is sandwiched by two S-atom ones (Fig. 17). From the previous theoretical studies [185–187], the electronic states close to  $E_F$  are predominantly contributed from the  $(4d_{z^2}, 4d_{xy}, 4d_{x^2-y^2})$  orbitals of Mo atoms. The three-orbital tight-binding model is sufficient to describe the essential electronic properties. In the bases of  $\{|4d_{z^2}\rangle, |4d_{xy}\rangle, |4d_{x^2-y^2}\rangle\} \otimes$

$\{\uparrow, \downarrow\}$ , the Hamiltonian is given by

$$H = \sum_{\langle i \rangle, o, m} E_o C_{iom}^+ C_{iom} + \sum_{\langle i, j \rangle, o, o', m} \gamma_{oo'}^{\mathbf{R}_{ij}} C_{iom}^+ C_{jo'm} + \sum_{\langle i \rangle, o, o', m} \frac{\lambda_{soc}}{2} C_{iom}^+ C_{io'm} (L_{oo'}^z \sigma_{mm}^z), \quad (4)$$

where the first, second and third terms are, respectively, the site energy, the nearest-neighbor hopping integral and the on-site SOC ( $\lambda_{soc}=73$  meV). These interaction energies could be found in [188]. The site energies are distinct for the  $4d_{z^2}$  and  $(4d_{xy}, 4d_{x^2-y^2})$  orbitals, and this difference will result in the valley-dependent LLs. The SOC is only contributed by the z-component angular momentum ( $L^z$ ) and spin moment ( $\sigma^z$ ). This interaction occurs between  $|4d_{x^2-y^2}\rangle$  and  $|4d_{xy}\rangle$  with the same spin configuration, while it is independent of  $|4d_{z^2}\rangle$ . As to the magnetic Hamiltonian,  $2R_B$  Mo atoms in an enlarged unit cell can build a  $12R_B \times 12R_B$  Hermitian matrix.

The multi-orbital bondings and the SOC cause monolayer MoS<sub>2</sub> to exhibit the unusual electronic structure. A direct energy gap of 1.59 eV at the  $K$  or  $K'$  point, as shown in Fig. 18(a), is dominated by the site energies of distinct orbitals. The significant orbital hybridizations lead to the strong wave-vector dependence. The electronic states of parabolic bands near  $E_F$  are centered at the  $K$ ,  $K'$  and  $\Gamma$  points. Furthermore, the SOC can create the spin-split energy bands, e.g., the largest splitting energy is  $2\lambda_{soc}$  at the  $K$  and  $K'$  points. Whether there exist the splitting spin-up and spin-down energy bands is dependent on the components of  $4d_{x^2-y^2}$  and  $4d_{xy}$  orbitals. The contributions of these two orbitals, as indicated in Figs. 18(b) and 18(c), are comparable in the splitting valence bands near the  $K$  and  $K'$  points. However, when the electronic states mainly come from one of them, or the  $4d_{z^2}$  orbital, the spin splitting is very weak, e.g., the lower-lying conduction bands in Fig. 18(d). It is also noticed that the IV-group systems do not have the spin-split energy bands as a result of the mirror symmetry in A and B sublattices (Figs. 7(a) and 10(a)).



MoS<sub>2</sub> systems exhibit the novel magnetic quantization, since the valley- and spin-dependent LL subgroups could survive simultaneously. All the LLs have two degenerate localization centers, the 1/2 and 2/2 localization centers in an enlarged unit cell, e.g., the 1/2 localized LL wavefunctions shown in Figs. 19(b) and 20(b). The dominating modes have the well-behaved spatial probability distributions. Each mode is fully determined by the spin-up or spin-down configuration, but not a superposition of two opposite spins as revealed in IV-group systems (Figs. 8(b), 8(d) and 10(e)). Each LL group of monolayer MoS<sub>2</sub> only corresponds to the occupied LLs or the unoccupied LLs, while that in IV-group systems includes the valence and conduction ones. It is further split into LL subgroups under the destruction of the spin and/or valley degeneracy.

As to the valence LLs, they are magnetically quantized from the electronic states centered at the  $\Gamma$ ,  $K$  and  $K'$  points (Fig. 19(a)). The  $\Gamma$ -dependent LL wavefunctions are independent of spin configuration (Fig. 19(b)), mainly owing to the  $d_{z^2}$ -orbital dominance and the almost vanishing SOC. The LL energies linearly grow with  $B_z$  (the blue curves in Fig. 19(a)), directly reflecting the parabolic dispersion near the  $\Gamma$  point. The similar  $B_z$ -dependence is revealed in the energy spectra of other LL subgroups. However, the spin-up and spin-down (spin-down & spin-up) LL subgroups, which come from the  $K$  ( $K'$ ) valley, are initiated at  $-0.792$  eV and  $-0.938$  eV, respectively. The spin-split LL subgroups are closely related to the  $4d_{x^2-y^2}$ - and  $4d_{xy}$ -dominated SOC's, as indicated in Figs. 18(b) and 18(c). Specifically, the degeneracy of two valleys is clearly destroyed in the increase of  $B_z$ . That is to say, there also exist the  $K$ - and  $K'$ -dependent LL subgroups, as shown in Fig. 19(a). The energy spacing is observable for a sufficiently high  $B_z$ , e.g.,  $\sim 15$  meV between the  $n_{K,\uparrow}^v=0$  and  $n_{K',\downarrow}^v$  LLs at  $B_z=40$  T. By the detailed analysis, the site-energy differences

in the  $B_z$ -enlarged unit cell is responsible for these LL subgroups [22]. The coexistence of the spin- and valley-dependent LL subgroups is absent in IV-group systems. On the other hand, the lower-lying conduction LLs exhibit the significantly  $K$ - and  $K'$ -dependent subgroups, and the very weak splittings in the spin-dependent subgroups (Fig. 20).

Up to now, STS has served as a powerful experimental method for investigating the magneto-electronic energy of the layered graphenes. The measured tunneling differential conductance ( $dI/dV$ ) is approximately proportional to DOS, and it directly reflects the structure, energy, number and height of the LL peaks. Part of theoretical predictions on the LL energy spectra are confirmed by STS measurements, such as, the  $\sqrt{B_z}$ -dependent LL energy in monolayer graphene [180–184], the linear  $B_z$ -dependence in AB-stacked bilayer graphene [189,190], the coexistent square-root and linear  $B_z$ -dependences in trilayer ABA stacking [191], and the 3D and 2D characteristics of the Landau subbands in AB-stacked graphite [192]. The other unusual magneto-electronic properties in the layered systems could be further verified using STS, including the normal and abnormal  $B_z$ -dependences in ABC-stacked graphenes, three kinds of LLs in sliding stacking systems, the SOC-induced spin-dominated LLs in germanene and silicene, two groups of low-lying LLs in tinene, the spin- and valley-dependent LLs in  $\text{MoS}_2$ , the special  $n^{c,v}$ - and  $B_z$ -dependence of LL energies in few-layer phosphorene, and the  $B_z$ - and  $V_z$ -dependent energy spectra with the LL splittings, crossings and anti-crossings. The STS examinations can provide the critical informations in the lattice symmetry, stacking configuration, SOC, and single- or multi-orbital hybridization.

## VI. CONCLUDING REMARKS

In this review work, the generalized tight-binding model, based on the subenvelope functions of distinct sublattices, is developed to explore the feature-rich magneto-electronic properties of layered systems. Such model is suitable for the various symmetric lattices, the multi-layer structures, the low-symmetry stacking configurations, the distinct dimensions, the multi-orbital bondings, the coupling interactions of orbital and spin, the composite external fields, and the uniform and modulated fields [50–53]. It is useful in understanding the essential physical properties, e.g., the diverse magneto-optical selection rules [13, 21, 26, 28, 50] and the LL-induced plasmons [5, 29, 30]. Moreover, this method could be further used to solve the new Hamiltonians of the emerging materials under the external fields.

The layered systems exhibit the unusual energy bands and the rich LLs in terms of the spatial distributions, orbital components, spin configurations, state degeneracy, and external-field dependences. The well-behaved, perturbed and undefined LLs are revealed in sliding graphenes, especially for the third ones mainly coming from the dramatic transformation between two high-symmetry stacking configurations. For the ABC- and AAB-stacked graphenes, the complicated interlayer hopping integrals result in the abnormal  $n^{c,v}$  ordering and the non-monotonic  $B_z$ -dependence. The intragroup and intergroup LL anti-crossings occur frequently, clearly illustrating the strong competition of the constant-energy loops in the magnetic quantization. The SOC can create the up- and down-dominated LLs in silicene, germanene, tinene and  $\text{MoS}_2$ . Tinene and  $\text{MoS}_2$  have the low-lying LLs composed of the different orbitals and spin configurations, mainly owing to the cooperation of the critical multi-orbital bondings and SOC. Concerning few-layer phosphorene, the puckered structure induces the intralayer and the interlayer multi-hopping integrals and thus the special dependence of LL energies on  $(n^{c,v}, B_z)$ . The LL state degeneracy is reduced,

when the inversion symmetry of  $z \rightarrow -z$  ( $x \rightarrow -x$ ) is destroyed, or two equivalent valleys are absent. For example, there are four-fold degenerate LLs in AAB-stacked graphene and few-layer phosphorene, and doubly degenerate  $n_{\Gamma}^{c,v}$  LLs in tinene. Specifically,  $\text{MoS}_2$  exhibits the spin- and valley-dependent LL subgroups, in which they arise from the SOC and the site-energy differences in the  $B_z$ -enlarged cell, respectively. The LL splittings are easily observed in the presence of a perpendicular electric field except for the AA-stacked graphenes and monolayer slicene. Furthermore, they induce the frequent anti-crossings and crossings in the  $V_z$ -dependent energy spectra. The two anti-crossing LLs, which are, respectively, associated with the interlayer hopping integrals and the significant SOC, have the quantum number differences of  $\Delta n=1$  and  $3I$ . The above-mentioned diverse LL energy spectra are directly reflected in the structure, height, energy and number of the prominent DOS peaks; furthermore, they could be verified by the STS measurements.

Also, the different dimensions can diversify the magnetic quantization. The 3D graphites and 1D graphene nanoribbons are very different from the 2D graphenes in the quantized electronic properties. As to graphites, the periodical interlayer hopping integrals induce the Landau subbands with energy dispersions along  $\hat{k}_z$ . The AA-, AB- and ABC-stacked graphites, respectively, possess one group, two groups, and one group of valence and conduction Landau subbands, in which the band widths are about 1 eV, 0.2 eV and 0.01 eV [2,6,196,197]. However, there are  $N$  groups of LLs in  $N$ -layer graphene systems. The AA- and ABC-staked graphites exhibit the monolayer-like wave functions, while the AB-stacked graphite displays the monolayer- and bilayer-like spatial distributions. In sharp contrast to the ABC-stacked graphenes, the anti-crossing phenomena in the  $B_z$ -dependent energy spectrum are absent in the rhombohedral graphite. On the other hand, the magneto-electronic

properties of graphene nanoribbons are mainly determined by the rather strong competition between the magnetic quantization and the finite-width quantum confinement [13]. When ribbon widths are larger than magnetic lengths, 1D nanoribbons have many composite energy subbands. Each subband is composed of a dispersion-less quasi-LL (QLL) and parabolic dispersions along  $\hat{k}_x$ . Such QLLs belong to the well-behaved modes localized at the ribbon center. Their magneto-optical selection rule is similar to that of monolayer graphene. In addition, a carbon nanotube could be regarded as a rolled-up graphene tubule. Except for a super-high magnetic field ( $B_z > 10^5$  T; [198]), it is impossible to generate the quantized QLLs in a curved cylinder because of the vanishing net magnetic flux.

## ACKNOWLEDGMENT

This work was supported by the NSC of Taiwan, under Grant No. NSC 102-2112-M-006-007-MY3.

\*e-mail address: mflin@mail.ncku.edu.tw

\*e-mail address: yarst5@gmail.com

# References

- [1] C. P. Chang, C. L. Lu, F. L. Shyu, R. B. Chen, Y. C. Huang, and M. F. Lin, "Magnetoelectronic properties of AB-stacked graphite", Carbon **43**, 1424-1431 (2005).
- [2] Y. H. Ho, J. Wang, Y. H. Chiu, M. F. Lin, and W. P. Su, "Characterization of Landau subbands in graphite: A tight-binding study", Phys. Rev. B **83**, 121201 (2011).
- [3] J. Wang, Y. H. Chiu, Y. H. Ho, T. S. Li, M. F. Lin, "Exact diagonalization of Landau levels in Bernal graphite", Solid State Commun. **151**, 1410-1414 (2011).
- [4] C. H. Ho, Y. H. Ho, Y. Y. Liao, Y. H. Chiu, C. P. Chang, M. F. Lin, "Diagonalization of Landau Level Spectra in Rhombohedral Graphite", J. Phys. Soc. Jpn. **81**, 024701 (2012).
- [5] R. B. Chen, C. W. Chiu, and M. F. Lin, Magnetoplasmons in simple hexagonal graphite", RSC Adv. **5**, 53736-53740 (2015).
- [6] C. H. Ho, C. P. Chang, and M. F. Lin, " Landau subband wave functions and chirality manifestation in rhombohedral graphite", Solid State Communications **197**, 11-15 (2014).
- [7] Y. K. Huang, S. C. Chen, Y. H. Ho, C. Y. Lin and M. F. Lin, "Feature-Rich Magnetic Quantization in Sliding Bilayer Graphenes", Sci. Rep. **4**, 7509 (2014).
- [8] J. H. Ho, Y. H. Lai, Y. H. Chiu, and M. F. Lin, "Landau levels in graphene", Physica E **40**, 1722-1725 (2008).
- [9] C. Y. Lin, J. Y. Wu, Y. H. Chiu and M. F. Lin, "Stacking-dependent magneto-electronic properties in multilayer graphenes", Phys. Rev. B **90**, 205434 (2014).

- [10] Y. H. Lai, J. H. Ho, C. P. Chang, and M. F. Lin, "Magnetoelectronic properties of bilayer Bernal graphene", Phys. Rev. B **77**, 085426(10) (2008).
- [11] C. Y. Lin, J. Y. Wu, Y. J. Ou, Y. H. Chiu, and M. F. Lin, "Magneto-electronic properties of multilayer graphenes", Phys. Chem. Chem. Phys. **17**, 26008-26035 (2015).
- [12] T. N. Do, P. H. Shih, C. P. Chang, C. Y. Lin, and M. F. Lin, "Rich Magneto-absorption Spectra in AAB-stacked Trilayer Graphene", Carbon **94**, 619-632 (2015).
- [13] Y. C. Huang, C. P. Chang, and M. F. Lin, "Magnetic and quantum confinement effects on electronic and optical properties of graphene ribbons", Nanotechnology **18**, 495401 (2007).
- [14] Y. C. Huang, C. P. Chang, W. S. Su, and M. F. Lin, "Low-energy Landau levels of Bernal zigzag graphene ribbons", J. Appl. Phys. **106**, 013711 (2009).
- [15] H. C. Chung, C. P. Chang, C. Y. Lin, and M. F. Lin, "Electronic and Optical Properties of Graphene Nanoribbons in External Fields", Phys. Chem. Chem. Phys. **18** (2016).
- [16] S. C. Chen, C. L. Wu, J. Y. Wu, M. F. Lin, "Novel Magnetic Quantization of  $sp^3$  Bonding in Monolayer Tinene", arXiv:1512.02129 (2015).
- [17] J. Y. Wu, C. Y. Lin, G. Gumbs and M. F. Lin, "The effect of perpendicular electric field on Temperature-induced plasmon excitations for intrinsic silicene", RSC Adv. **5**, 51912-51918 (2015).
- [18] J. Y. Wu, S. C. Chen, and M. F. Lin, "Temperature-dependent Coulomb excitations in silicene", New J. Phys. **16**, 125002 (2014).

- [19] J. Y. Wu, S. C. Chen, G. Gumbs, M. F. Lin, "Feature-rich electronic excitations in external fields of 2D silicene", arXiv: 1510.01504v1 (2015).
- [20] Y. H. Ho, W. P. Su, and M. F. Lin, "Hofstadter spectra for d-orbital electrons: a case study on MoS<sub>2</sub>", RSC Advances, **5**, 20858-20864. (2015).
- [21] Y. H. Ho, C. W. Chiu, W. P. Su, M. F. Lin, "Magneto-optical spectra of transition metal dichalcogenides: a comparative study" Appl. Phys. Lett. **105**, 222411 (2014).
- [22] Y. H. Ho, Y. H. Wang, and H. Y. Chen, "Magnetoelectronic and optical properties of a MoS<sub>2</sub> monolayer" Phys. Rev. B **89**, 155316 (2014).
- [23] Y. C. Huang, C. P. Chang, and M. F. Lin, "Magnetoabsorption spectra of bilayer graphene ribbons with Bernal stacking", Phys. Rev. B **78**, 115422(9) (2008).
- [24] Y. P. Lin, C. Y. Lin, Y. H. Ho, T.N. Do and M. F. Lin, "Magneto-optical properties of ABC-stacked trilayer graphene", Phys. Chem. Chem. Phys. **17**, 15921-15927 (2015).
- [25] R. B. Chen, Y. H. Chiu, M. F. Lin, "Beating oscillations of magneto-optical spectra in simple hexagonal graphite", Comput. Phys. Commun. **189**, 60-65 (2014).
- [26] R. B. Chen, Y. H. Chiu, and M. F. Lin, "A theoretical evaluation of the magneto-optical properties of AA-stacked graphite", Carbon **54**, 248-276 (2012).
- [27] Y. H. Ho, J. Y. Wu, R. B. Chen, Y. H. Chiu, and M. F. Lin, "Optical transitions between Landau levels: AA-stacked bilayer graphene", Appl. Phys. Lett., **97**, 101905 (2010).
- [28] Y. H. Ho, Y. H. Chiu, D. H. Lin, C. P. Chang, and M. F. Lin, "Magneto-optical selection rules in bilayer Bernal graphene", ACS Nano **4**, 1465-1472 (2010).



- [29] J. Y. Wu, Godfrey Gumbs, and M. F. Lin, "Combined effect of stacking and magnetic field on plasmon excitations in bilayer graphene", *Phys. Rev. B* **89**, 165407 (2014).
- [30] J. Y. Wu, S. C. Chen, Oleksiy Roslyak, Godfrey Gumbs, M. F. Lin, "Plasma Excitations in Graphene: Their Spectral Intensity and Temperature Dependence in Magnetic Field", *ACS Nano*. **5**, 1026-1032 (2011).
- [31] Y. P. Lin, C. Y. Lin, C. P. Chang, and M. F. Lin, "Electric-field-induced rich magneto-absorption spectra of ABC-stacked trilayer graphene", *RSC Adv.* **5**, 80410 (2015).
- [32] Yisong Zheng and Tsuneya Ando, "Hall conductivity of a two-dimensional graphite system", *Phys. Rev. B* **65**, 245420 (2002).
- [33] S. G. Sharapov, V. P. Gusynin, and H. Beck, "Magnetic oscillations in planar systems with the Dirac-like spectrum of quasiparticle excitations", *Phys. Rev. B* **69**, 075104 (2004).
- [34] V. P. Gusynin, and S. G. Sharapov, "Unconventional Integer Quantum Hall Effect in Graphene", *Phys. Rev. Lett.* **95**, 146801 (2005).
- [35] M. O. Goerbig, "Electronic properties of graphene in a strong magnetic field" *Rev. Mod. Phys.* **83**, 1193-1243 (2011).
- [36] C. P. Chang, "Exact solution of the spectrum and magneto-optics of multilayer hexagonal graphene", *J. Appl. Phys.* **110**, 013725 (2011).
- [37] E. McCann and V. I. Fal'ko, "Landau-Level Degeneracy and Quantum Hall Effect in a Graphite Bilayer", *Phys. Rev. Lett.* **96**, 086805 (2006).

- [38] M. Koshino and E. McCann, "Landau level spectra and the quantum Hall effect of multilayer graphene", *Phys. Rev. B* **83**, 165443 (2011).
- [39] H. Min and A. H. MacDonald, "Chiral decomposition in the electronic structure of graphene multilayers", *Phys. Rev. B* **77**, 155416 (2008).
- [40] S. H. R. Sena, J. M. Jr. Pereira, F. M. Peeters and G. A. Farias, "Landau levels in asymmetric graphene trilayers", *Phys. Rev. B* **84**, 205448 (2011).
- [41] E. McCann and M. Koshino, "The electronic properties of bilayer graphene", *Rep. Prog. Phys.* **76**, 056503 (2013).
- [42] M. Ezawa, "Valley-polarized metals and quantum anomalous Hall effect in silicene", *Phys. Rev. Lett.* **109**, 055502 (2012).
- [43] M. Tahir, P. Vasilopoulos, and F. M. Peeters, "Quantum magnetotransport properties of a MoS<sub>2</sub> monolayer" *Phys. Rev. B* **93**, 035406 (2016).
- [44] A. S. Rodin, A. Carvalho, and A. H. Castro Neto, "Strain-Induced Gap Modification in Black Phosphorus", *Phys. Rev. Lett.* **112**, 176801 (2014).
- [45] T. S. Li, S. C. Chang, J. Y. Lien, and M. F. Lin, "Electronic properties of nanotube-ribbon hybrid systems", *Nanotechnology* **19**, 105703(6) (2008).
- [46] T. S. Li, M. F. Lin, and S. C. Chang, "Quantum conductance in nanotube-ribbon hybrids", *J. Appl. Phys.* **107**, 063714(8) (2010).
- [47] C. H. Lee, S. C. Chen, C. K. Yang, W. S. Su, and M. F. Lin, "Low-energy electronic structures of nanotube-nanoribbon hybrid systems", *Comput. Phys. Commun.* **182**, 68–70 (2011).

- [48] C. H. Lee, C. K. Yang, M. F. Lin, C. P. Chang, and W. S. Su, "Structural and Electronic Properties of Graphene Nanotube-Nanoribbon Hybrids", *Phys. Chem. Chem. Phys.* **13**, 3925-3931 (2011).
- [49] M. H. Lee, H. C. Chung, J. M. Lu, C. P. Chang, and M. F. Lin, "Electronic and optical properties in graphane", *Philos. Mag.* **95**, 2717-2730 (2015).
- [50] Y. C. Ou, Y. H. Chiu, P. H. Yang and M. F. Lin, "The selection rule of graphene in a composite magnetic field", *Optics Express* **22**, 7473 (2014).
- [51] Y. C. Ou, Y. H. Chiu, J. M. Lu, W. P. Su, M. F. Lin, "Electric modulation effect on magneto-optical spectrum of monolayer graphene", *Comput. Phys. Commun.* **184**, 1821-1826 (2013).
- [52] Y. C. Ou, J. K. Sheu, Y. H. Chiu, R. B. Chen, M. F. Lin, "Influence of modulated fields on the Landau level properties of graphene", *Phys. Rev. B* **83**, 195405 (2011).
- [53] Y. H. Chiu, Y. C. Ou, Y. Y. Liao, and M. F. Lin, "Optical-absorption spectra of single-layer graphene in a periodic magnetic field", *J. Vac. Sci. Technol. B* **28**, 386-390 (2010).
- [54] B. Radisavljevic, A. Radenovic, J. Brivio, V. Giacometti, A. Kis, "Single-layer MoS<sub>2</sub> transistors" *Nature Nanotech.* **6**, 147-150 (2011).
- [55] K. Hao, G. Moody, F. Wu, C. Dass, L. Xu, C. H. Chen, M. Y. Li, L. J. Li, A. MacDonald and X. Li, "Direct Measurement of Exciton Valley Coherence in Monolayer WSe<sub>2</sub>" *Nature Phys.* (2016).

- [56] C. Zhang, Y. Chen, J. K. Huang, X. Wu, L. J. Li, W. Yao, J. Tersoff and C. K Shih, "Visualizing Band Offsets and Edge States in Bilayer-Monolayer Transition Metal Dichalcogenides Lateral Heterojunction" Nat. Commun. **7**, 10349, (2016).
- [57] HN Li, YM Shi, MH Chiu and LJ Li, "Emerging energy applications of two-dimensional layered transition metal dichalcogenides" NANO ENERGY **18**, 293-305 (2015).
- [58] W. T. Hsu, Y. L. Chen, C. H. Chen, P. S. Liu, T. H. Hou, L. J. Li, and W. H. Chang, "Optically Initialized Robust Valley-Polarized Holes in Monolayer WSe<sub>2</sub>" Nature Comm. **6**, 8963 (2015).
- [59] J. Qi, Y. W. Lan, A. Stieg, J. H. Chen, Y. L. Zhong, L. J. Li, C. D. Chen, Y. Zhang, and K. Wang, "Piezoelectric effect in CVD-grown atomic-monolayer triangular MoS<sub>2</sub> piezotronics" Nature Comm. **6**, 7430 (2015).
- [60] M. Engel, M. Steiner, A. Lombardo, AC Ferrari, v. Lohneysen H., P. Avouris, et al., "Light matter interaction in a micro-cavity controlled graphene transistor" Nat. Commun. **3**, 906-11 (2012).
- [61] F. Khan, SH Baek, and JH. Kim, "One-step and controllable bipolar doping of reduced graphene oxide using TMAH as reducing agent and doping source for field effect transistors" Carbon **100**, 608-16 (2016).
- [62] A. Kumar, P. Tyagi, J. Dagar, and R. Srivastava, "Tunable field effect properties in solid state and flexible graphene electronics on composite high-low k dielectric" Carbon **99**, 579-84 (2016).

- [63] MY Li, Y. Shi, CC Cheng, LS Lu, YC Lin, and HL Tang, et al., "Epitaxial growth of a monolayer WSe<sub>2</sub>-MoS<sub>2</sub> lateral p-n junction with an atomically sharp interface", Science **349**, 524-58 (2015).
- [64] Y.-T. Wang, C.-W. Luo, A. Yabushita, K. H. Wu, T. Kobayashi, C.-H. Chen, and L.-J. Li "Ultrafast Multi-Level Logic Gates with Spin-Valley Coupled Polarization Anisotropy in Monolayer MoS<sub>2</sub>" Sci. Rep. **5**, 8289 (2015)
- [65] A. Kasry, MA Kuroda, GJ Martyna, GS Tulevski, and AA Bol "Chemical Doping of Large-Area Stacked Graphene Films for Use as Transparent Conducting Electrodes", ACS NANO **4**, 3839-3844 (2010).
- [66] Q. Xiang, J. Yu, and M. Jaroniec, "Graphene-based semiconductor photocatalysts", Chem. Soc. Rev. **41**, 782-796 (2012).
- [67] MC Rechtsman, J. M. Zeuner, Y. Plotnik, Y. Lumer, D. Podolsky, F. Dreisow, S. Nolte, M. Segev and A. Szameit, "Photonic Floquet topological insulators", NATURE **496**, 196-200 (2013).
- [68] F. H. L. Koppens, T. Mueller, Ph. Avouris, A. C. Ferrari, M. S. Vitiello, and M. Polini, "Photodetectors based on graphene, other two-dimensional materials and hybrid systems", Nat. Nanotechnol. **9**, 780 (2014).
- [69] F. Bonaccorso, Z. Sun, T. Hasan, A. C. Ferrari., "Graphene photonics and optoelectronics", Nat. Photonics **4**, 611 (2010).

- [70] S. F. Tseng, W. T. Haiso, P. Y. Cheng, C. K. Chung, Y. S. Lin, S. C. Chien, et al., "Graphene-based chips fabricated by ultraviolet laser patterning for an electrochemical impedance spectroscopy", *Sens. actuators. B Chem.* **226**, 342 (2016).
- [71] J. B. Liu, P. J. Li, Y. F. Chen, X. B. Song, Q. Mao, Y. Wu, et al., "Flexible terahertz modulator based on coplanar-gate graphene field-effect transistor structure", *Opt. Lett.* **41**, 816 (2016).
- [72] H. Y. Deng, X. F. Chen, B. A. Malomed, N. C. Panoiu, F. W. Ye, "Tunability and Robustness of Dirac Points of Photonic Nanostructures", *IEEE J. Sel. Topics Quantum Electron.* **22**, 5000509 (2016).
- [73] H. G. Yan, X. S. Li, B. Chandra, G. Tulevski, Y. G. Wu, M. Freitag, W. J. Zhu, P. Avouris, and F. G. Xia, "Tunable infrared plasmonic devices using graphene/insulator stacks" *Nat. Nanotechnol.* **7**, 330 (2012).
- [74] S. Kocaman, M. S. Aras, P. Hsieh, J. F. McMillan, C. G. Biris, N. C. Panoiu, M. B. Yu, D. L. Kwong, A. Stein, and C. W. Wong, "Zero phase delay in negative-refractive-index photonic crystal superlattices", *Nat. Photonics* **5**, 499 (2011).
- [75] P. Tassin, T. Koschny, and C. M. Soukoulis, "Graphene for Terahertz Applications" *Science* **341**, 620 (2013).
- [76] A. Vakil, and N. Engheta, "Transformation Optics Using Graphene", *Science* **332**, 1291 (2011).

- [77] H. Y. Deng, F. W. Ye, B. A. Malomed, X. F. Chen, N. C. Panoiu, "Spin-dependent refraction at the atomic step of transition-metal dichalcogenides", *Phys. Rev. B* **91**, 201402 (2015).
- [78] H. Y. Deng, X. F. Chen, B. A. Malomed, N. C. Panoiu, and F. W. Ye, "Transverse Anderson localization of light near Dirac points of photonic nanostructures", *Sci. Rep.* **5**, 15585 (2015).
- [79] G. de Abajo, and F. Javier, "Graphene Plasmonics: Challenges and Opportunities", *ACS Photonics* **1**, 135 (2014).
- [80] I. Shown, H. C. Hsu, Y. Chang, C. H. Lin, P. K. Roy, A. Ganguly, et al., "Highly Efficient Visible Light Photocatalytic Reduction of CO<sub>2</sub> to Hydrocarbon Fuels by Cu-Nanoparticle Decorated Graphene Oxide", *Nano Lett.* **14**, 6097 (2014).
- [81] H. C. Hsu, I. Shown, H. Y. Wei, Y. C. Chang, H. Y. Du, Y. G. Lin, et al., "Graphene oxide as a promising photocatalyst for CO<sub>2</sub> to methanol conversio", *Nanoscale* **5**, 262 (2013).
- [82] G. Ibram, "Electrochemical conversion of carbon dioxide into renewable fuel chemicals-The role of nanomaterials and the commercialization", *RENEW. SUST. ENERG. REV.* **59**, 1269 (2016).
- [83] R. H. Baughman, A. A. Zakhidov, and W. A. de Heer, "Carbon Nanotubes—the Route Toward Applications", *Science* **297**, 787 (2002).
- [84] P. Simon, and Y. Gogotsi, "Materials for electrochemical capacitors", *Nat. Mat.* **7**, 845 (2008).

- [85] M. D. Stoller, S. J. Park, Y. W. Zhu, J. H. An, and R. S. Ruoff, "Graphene-Based Ultracapacitors" *Nano Lett.* **8**, 3498-502 (2008).
- [86] C. K. Chan, H. L. Peng, G. Liu, K. McIlwrath, X. F. Zhang, R. A. Huggins, Y. Cui, "High-performance lithium battery anodes using silicon nanowires", *Nat. Nanotechnol* **3**, 31 (2008).
- [87] G. P. Wang, L. Zhang, and J. J. Zhang, "A review of electrode materials for electrochemical supercapacitors" *Chem. Soc. Rev.* **41**, 797 (2012).
- [88] L. G. Bulusheva, V. E. Arkhipov, E. O. Fedorovskaya, S. Zhang, A. G. Kurennya, M. A. Kanygin, I. P. Asanov, A. R. Tsygankova, X. H. Chen, H. H. Song, "Fabrication of free-standing aligned multiwalled carbon nanotube array for Li-ion batteries", *J. Power Sources* **311**, 42 (2016).
- [89] M. A. Bissett, S. D. Worrall, I. A. Kinloch, and R. A. W. Dryfe, "Comparison of Two-Dimensional Transition Metal Dichalcogenides for Electrochemical Supercapacitors", *Electrochim. Acta* **201**, 30 (2016).
- [90] J. Y. Li, L. Wang, and X. M. He, "Phosphorus-Based Composite Anode Materials for Secondary Batteries", *Prog. Chem.* **28**, 193 (2016).
- [91] Y. G. Sun, Q. Wu, and G. Q. Shi, "Graphene based new energy materials", *Energy Environ. Sci.* **4**, 1113 (2011).
- [92] H. Gwon, H. S. Kim, K. U. Lee, D. H. Seo, Y. C. Park, Y. S. Lee, B. T. Ahn, and K. Kang, "Flexible energy storage devices based on graphene paper", *Energy Environ. Sci.* **4**, 1277 (2011).



- [93] Y. K. Yang, C. P. Han, B. B. Jiang, J. Iocozzia, C. G. He, D. Shi, T. Jiang, and Z. Q. Lin, "Flexible energy storage devices based on graphene paper", *Mater. Sci. Eng. R-Rep.* **102**, 1 (2016).
- [94] S. Hattendorf, A. Georgi, M. Liebmann, and M. Morgenstern, "Networks of ABA and ABC stacked graphene on mica observed by scanning tunneling microscopy", *Surf. Sci.* **610**, 53 (2013).
- [95] K. S. Novoselov, A. K. Geim, S. V. Morozov, D. Jiang, Y. Zhang, S. V. Dubonos and A. A. Firsov, "Electric Field Effect in Atomically Thin Carbon Films", *Science* **306**, 666 (2004).
- [96] B. Jayasena, and S. Subbiah, "A novel mechanical cleavage method for synthesizing few-layer graphenes", *Nanoscale Res. Lett.* **6**, 95 (2011).
- [97] A. J. Cooper, N. R. Wilson, I. A. Kinloch, and R. A. W. Dryfe, "Single stage electrochemical exfoliation method for the production of few-layer graphene via intercalation of tetraalkylammonium cations", *Carbon* **66**, 340 (2014).
- [98] M. Noroozi, A. Zakaria, S. Radiman, and Z. A. Wahab, "Environmental Synthesis of Few Layers Graphene Sheets Using Ultrasonic Exfoliation with Enhanced Electrical and Thermal Properties", *PLOS ONE* **11**, e0152699 (2016).
- [99] M. Dobbelin, A. Ciesielski, S. Haar, S. Osella, M. Bruna, A. Minoia, et al., "Light-enhanced liquid-phase exfoliation and current photoswitching in graphene-zobenzene composites", *Nat. Commun.* **7**, 11090 (2016).

- [100] S. Majee, M. Song, S. L. Zhang, and Z. B. Zhang, "Scalable inkjet printing of shear-exfoliated graphene transparent conductive films", *Carbon* **102**, 51 (2016).
- [101] Y. Arao, Y. Mizuno, K. Araki, and M. Kubouchi, "Mass production of high-aspect-ratio few-layer-graphene by high-speed laminar flow", *Carbon* **102**, 330 (2016).
- [102] M. V. Bracamonte, G. I. Lacconi, S. E. Urreta, and L. E. F. Foa Torres, "On the Nature of Defects in Liquid-Phase Exfoliated Graphene", *J. Phys. Chem. C* **118**, 15455 (2014).
- [103] P. Song, X. Zhang, M. Sun, X. Cui, and Y. Lin, "Synthesis of graphene nanosheets via oxalic acid-induced chemical reduction of exfoliated graphite oxide", *RSC Adv.* **2**, 1168 (2012).
- [104] L. Dou, F. Cui, Y. Yu, G. Khanarian, S. W. Eaton, Q. Yang, J. Resasco, et al., "Solution-Processed Copper/Reduced-Graphene-Oxide Core/Shell Nanowire Transparent Conductors", *ACS Nano*. **10**, 2600 (2016).
- [105] L. J. Yin, W. X. Wang, K. K. Feng, J. C. Nie, C. M. Xiong, R. F. Dou, et al., "Liquid-assisted tip manipulation: fabrication of twisted bilayer graphene superlattices on HOPG", *Nanoscale* **7**, 14865 (2015).
- [106] P. Xu, M. L. Ackerman, S. D. Barber, J. K. Schoelz, D. J. Qi, P. M. Thibado, et al., "Graphene Manipulation on 4H-SiC(0001) Using Scanning Tunneling Microscopy", *Jpn. J. Appl. Phys.* **52**, 035104 (2013).

- [107] P. Xu, Y. R. Yang, D. Qi, S. D. Barber, J. K. Schoelz, M. L. Ackerman, et al., "Electronic transition from graphite to graphene via controlled movement of the top layer with scanning tunneling microscopy", *Phys. Rev. B* **86**, 085428 (2012).
- [108] Y. I. Kurys, O. O. Ustavytska, V. G. Koshechko, and V. D. Pokhodenko, "Structure and electrochemical properties of multilayer graphene prepared by electrochemical exfoliation of graphite in the presence of benzoate ions", *RSC Adv.* **6**, 36050 (2016).
- [109] P. Xu, M. L. Ackerman, S. D. Barber, J. K. Schoelz, P. M. Thibado, V. D. Wheeler, et al., "Competing scanning tunneling microscope tip-interlayer interactions for twisted multilayer graphene on the a-plane SiC surface", *Sur. Sci.* **617**, 113 (2013).
- [110] S. Ye, and W. C. Oh, "Demonstration of enhanced the photocatalytic effect with PtSe<sub>2</sub> and TiO<sub>2</sub> treated large area graphene obtained by CVD method", *Mat. Sci. Semicon. Proc.* **48**, 106 (2016).
- [111] W. Norimatsu, and M. Kusunoki, "Selective formation of ABC-stacked graphene layers on SiC(0001)", *Phys. Rev. B* **81**, 161410 (2010).
- [112] J. H. Warner, M. Mukai, and A. I. Kirkland, "Atomic Structure of ABC Rhombohedral Stacked Trilayer Graphene", *ACS Nano* **6**, 5680 (2012).
- [113] L. B. Biedermann, M. L. Bolen, M. A. Capano, D. Zemlyanov, and R. G. Reifemberger, "Insights into few-layer epitaxial graphene growth on 4H-SiC(000 $\bar{1}$ ) substrates from STM studies", *Phys. Rev. B* **79**, 125411 (2009).

- [114] J. Borysiuk, J Soltys, and J Piechota, "Stacking sequence dependence of graphene layers on SiC (000 $\bar{1}$ ) - experimental and theoretical investigation", J. Appl. Phys. **109**, 093523 (2011).
- [115] A. Reina, X. Jia, J. Ho, D. Nezich, H. Son, V. Bulovic, et al., "Large Area, Few-Layer Graphene Films on Arbitrary Substrates by Chemical Vapor Deposition", Nano Lett. **9**, 30 (2009).
- [116] L. Liu, H. Zhou, R. Cheng, W. J. Yu, Y. Liu, Y. Chen, et al., "High-Yield Chemical Vapor Deposition Growth of High-Quality Large-Area AB-Stacked Bilayer Graphene", ACS Nano. **6**, 8241 (2012).
- [117] T. Gomez, E. Florez, J. A. Rodriguez, and F. Illas, "Reactivity of Transition Metals (Pd, Pt, Cu, Ag, Au) toward Molecular Hydrogen Dissociation: Extended Surfaces versus Particles Supported on TiC(001) or Small Is Not Always Better and Large Is Not Always Bad", J. Phys. Chem. C **115**, 11666 (2011).
- [118] X. Zhang, H. Li, and F. Ding, "Self-Assembly of Carbon Atoms on Transition Metal Surfaces-Chemical Vapor Deposition Growth Mechanism of Graphene", Adv. Mater. **26**, 5488 (2014).
- [119] Z. Zhou, B. F. Habenicht, and Q. Guo, "Graphene moiré structure grown on a pseudomorphic metal overlayer supported on Ru(0001)", Surf. Sci. **611**, 67 (2013).
- [120] K. S. Kim, Y. Zhao, H. Jang, S. Y. Lee, J. M. Kim, K. S. Kim, et al., "Large-scale pattern growth of graphene films for stretchable transparent electrodes", Nature **457**, 706 (2009).

- [121] X. Li, W. Cai, J. An, S. Kim, J. Nah, D. Yang, et al., "Large-Area Synthesis of High-Quality and Uniform Graphene Films on Copper Foils", *Science* **324**, 1312 (2009).
- [122] H. Zhou, W. J. Yu, L. Liu, R. Cheng, Y. Chen, X. Huang , et al., "Chemical vapour deposition growth of large single crystals of monolayer and bilayer graphene", *Nat. Commun.***4**, 2096 (2013).
- [123] C. Y. Su, A. Y. Lu, C. Y. Wu, Y. T. Li, K. K. Liu, W. Zhang, et al., "Direct Formation of Wafer Scale Graphene Thin Layers on Insulating Substrates by Chemical Vapor Deposition", *Nano Lett.* **11**, 3612 (2011).
- [124] S. Bae, H. Kim, Y. Lee, X. Xu, J. S. Park, Y. Zheng, et al., "Roll-to-roll production of 30-inch graphene films for transparent electrodes", *Nat. Nanotechnol.* **5**, 574 (2010).
- [125] R. K. Vijayaraghavan, C. Gaman, B. Jose, A. P. McCoy, T. Cafolla, P. J. McNally, et al., "Pulsed-Plasma Physical Vapor Deposition Approach Toward the Facile Synthesis of Multilayer and Monolayer Graphene for Anticoagulation Applications", *ACS Appl. Mater. Interfaces* **8**, 4878 (2016).
- [126] X. Y. Wu, G. F. Zhong, L. D'Arsie, H. Sugime, S. Esconjauregui, A. W. Robertson , et al., "Growth of Continuous Monolayer Graphene with Millimeter-sized Domains Using Industrially Safe Conditions", *Sci. Rep.* **6**, 21152 (2016).
- [127] A. Bosca, J. Pedros, J. Martinez, T. Palacios, and F. Calle, "Automatic graphene transfer system for improved material quality and efficiency", *Sci. Rep.* **6**, 21676 (2016).

- [128] J. K. Lee, S. C. Lee, J. P. Ahn, S. C. Kim, J. I. B. Wilson, and P. John, "The growth of AAAA graphite on (111) diamond", J. Chem. Phys. **129**, 234709 (2008).
- [129] Y. Que, W. Xiao, C. Hhen, D. Wang, S. Du, and H. J. Gao, "Stacking-dependent electronic property of trilayer graphene epitaxially grown on Ru(0001)", Appl. Phys. Lett. **107**, 263101 (2015).
- [130] T. Li, C. Eugenio, C. Daniele, G. Carlo, F. Marco, D. Madan, M. Alessandro, and A. Deji "Silicene field-effect transistors operating at room temperature", Nat. Nanotech. **10**, 227-231 (2015).
- [131] P. Vogt, P. D. Padova, C. Quaresima, J. Avila, E. Frantzeskakis, M. C. Asensio, A. Resta, B. Ealet, and G. L. Lay, "Silicene: Compelling Experimental Evidence for Graphenelike Two-Dimensional Silicon", Phys. Rev. Lett. **108**, 155501 (2012).
- [132] B. Aufray, A. Kara, S. Vizzini, H. Oughaddou, C. Landri, B. Ealet, and G. L. Lay "Graphene-like silicon nanoribbons on Ag(110): A possible formation of silicene" Appl. Phys. Lett. **96**, 183102 (2010).
- [133] A. Fleurence, R. Friedlein, T. Ozaki, H. Kawai, Y. Wang, and Y. Yamada-Takamura, "Experimental Evidence for Epitaxial Silicene on Diboride Thin Films" Phys. Rev. Lett. **108**, 245501 (2012).
- [134] L. Meng, Y. Wang, L. Zhang, S. Du, R. Wu, L. Li, Y. Zhang, G. Li, H. Zhou, W. A. Hofer and H. J. Gao, "Buckled Silicene Formation on Ir(111)" Nano Lett. **13**, 685-690 (2013).

- [135] L. F. Li, S. Z. Lu, J. B. Pan, Z. H. Qin, Y. Q. Wang, Y. L. Wang, G. Y. Cao, S. X. Du, and H. J. Gao "Buckled Germanene Formation on Pt(111)" *Adv. Mater.* **26**, 4820-4828 (2014).
- [136] M. Derivaz, D. Dentel, R. Stephan, M. C. Hanf, A. Mehdaoui, P. Sonnet, and C. Pirri "Continuous Germanene Layer on Al(111)" *Nano Lett.* **15**, 2510-2516 (2015).
- [137] M. E. Dávila, L. Xian, S. Cahangirov, A. Rubio, and G. L. Lay "Germanene: a novel two-dimensional germanium allotrope akin to graphene and silicene" *New J. Phys.* **16**, 095002 (2014).
- [138] C. C. Liu, H. Jiang, and Y. Yao, "Low-energy effective Hamiltonian involving spin-orbit coupling in silicene and two-dimensional germanium and tin", *Phys. Rev. B* **84**, 195430 (2011).
- [139] C. C. Liu, W. Feng, and Y. Yao, "Quantum Spin Hall Effect in Silicene and Two-Dimensional Germanium" *Phys. Rev. Lett.* **107**, 076802 (2011).
- [140] M. Ezawa, "A topological insulator and helical zero mode in silicene under an inhomogeneous electric field", *New J. Phys.* **14**, 033003 (2012).
- [141] N. D. Drummond, V. Zólyomi, and V. I. Fal'ko "Electrically tunable band gap in silicene", *Phys. Rev. B* **85**, 075423 (2012).
- [142] F. Zhu, W. Chen, Y. Xu, C. Gao, D. Guan, C. Liu, D. Qian, S. C. Zhang and J. Jia, "Epitaxial growth of two-dimensional stanene", *Nat. Mater.* **14**, 1020-1025 (2015).

- [143] Y. Xu, B. Yan, H.J. Zhang, J. Wang, G. Xu, P. Tang, W. Duan, and S. C. Zhang, "Large-Gap Quantum Spin Hall Insulators in Tin Films", *Phys. Rev. Lett.* **111**, 136804 (2013).
- [144] H. Liu, Y. Du, Y. Deng, and P. D. Ye, "Semiconducting black phosphorus: synthesis, transport properties and electronic applications", *Chem. Soc. Rev.* **44**, 2732 (2015).
- [145] L. Li, Y. Yu, G. J. Ye, Q. Ge, X. Ou, H. Wu, D. Feng, X. H. Chen, and Y. Zhang, "Black Phosphorus Field-Effect Transistors", *Nat. Nanotechnol.* **9**, 372 (2014).
- [146] H. Liu, A. T. Neal, Z. Zhu, Z. Luo, X. Xu, D. Tománek, and P. D. Ye, "Phosphorene: An Unexplored 2D Semiconductor with a High Hole Mobility", *ACS Nano* **8**, 4033 (2014).
- [147] J. R. Brent, N. Savjani, E. A. Lewis, S. J. Haigh, D. J. Lewis, and P. O'Brien, "Production of Few-Layer Phosphorene by Liquid Exfoliation of Black Phosphorus", *Chem. Commun.* **50**, 13338 (2014).
- [148] P. Yasaei, B. Kumar, T. Foroozan, C. Wang, M. Asadi, D. Tuschel, J. E. Indacochea, R. F. Klie, and A. Salehi-Khojin, "High-Quality Black Phosphorus Atomic Layers by Liquid-Phase Exfoliation", *Adv. Mater.* **27**, 1887 (2015).
- [149] J. Kang, J. D. Wood, S. A. Wells, J.-H. Lee, X. Liu, K. S. Chen, and M. C. Hersam, "Solvent Exfoliation of Electronic-Grade, Two-Dimensional Black Phosphorus", *ACS Nano* **9**, 3596 (2015).
- [150] S. Lange, P. Schmidt, and T. Nilges, "Au<sub>3</sub>SnP<sub>7</sub>@Black Phosphorus: An Easy Access to Black Phosphorus", *Inorg. Chem.* **46**, 4028 (2007).



- [151] T. Nilges, M. Kersting, and T. Pfeifer, "A fast low-pressure transport route to large black phosphorus single crystals", *J. Solid State Chem.* **181**, 1707 (2008).
- [152] M. Kopf, N. Eckstein, D. Pfister, C. Grotz, I. Kruger, M. Greiwe, T. Hansen, H. Kohlmann, and T. Nilges, "Access and in situ growth of phosphorene-precursor black phosphorus", *J. Cryst. Growth* **405**, 6 (2014).
- [153] L. Li, Y. Yu, G. J. Ye, Q. Ge, X. Ou, H. Wu, D. Feng, X. H. Chen, and Y. Zhang, "Black phosphorus field-effect transistors", *Nat. Nanotechnol.* **9**, 372 (2014).
- [154] A. N. Rudenko, and M. I. Katsnelson, "Quasiparticle band structure and tight-binding model for single- and bilayer black phosphorus", *Phys. Rev. B* **89**, 201408 (2014).
- [155] T. Low, A. S. Rodin, A. Carvalho, Y. Jiang, H. Wang, F. Xia, and A. H. Castro Neto, "Tunable optical properties of multilayer black phosphorus thin films", *Phys. Rev. B* **90**, 075434 (2014).
- [156] K. Dolui, and S. Y. Quek, "Quantum-confinement and Structural Anisotropy result in Electrically-Tunable Dirac Cone in Few-layer Black Phosphorous", *Sci. Rep.* **5**, 11699 (2015).
- [157] Q. Liu, X. Zhang, L. B. Abdalla, A. Fazzio, and A. Zunger, "Switching a Normal Insulator into a Topological Insulator via Electric Field with Application to Phosphorene", *Nano Lett.* **15**, 1222 (2015).

- [158] K. S. Novoselov, D. Jiang, F. Schedin, T. J. Booth, V. V. Khotkevich, S. V. Morozov and A. K. Geim, "Two-dimensional atomic crystals" *Proc. Natl. Acad. Sci. U. S. A.*, **102**, 10451 (2005).
- [159] Z. Y. Yin, H. Li, L. Jiang, Y.M. Shi, Y. H. Sun, G. Lu, Q. Zhang, X. D. Chen and H. Zhang "Single-Layer MoS<sub>2</sub> Phototransistors" *ACS Nano* **6**, 74 (2012).
- [160] H. Li, J. Wu, Z. Yin, and H. Zhang, "Preparation and Applications of Mechanically Exfoliated Single-Layer and Multilayer MoS<sub>2</sub> and WSe<sub>2</sub> Nanosheets" *Acc. Chem. Res.* **47**, 1067-1075 (2014).
- [161] K. F. Mak, C. Lee, J. Hone, J. Shan, and T. F. Heinz, "Atomically Thin MoS<sub>2</sub>: A New Direct-Gap Semiconductor" *Phys. Rev. Lett.* **105**, 136805 (2010).
- [162] J. N. Coleman, M. Lotya, A. O'Neill, S. D. Bergin, P. J. King, U. Khan et al., "Two-Dimensional Nanosheets Produced by Liquid Exfoliation of Layered Materials", *Science* **331**, 568-571 (2011).
- [163] K. G. Zhou, N. N. Mao, H. X. Wang, Y. Peng and H. L. Zhang, "A Mixed-Solvent Strategy for Efficient Exfoliation of Inorganic Graphene Analogues" *Angew. Chem. Int. Ed.* **50**, 10839 (2011).
- [164] Y. H. Lee, X. Q. Zhang, W. Zhang, M. T. Chang, C. T. Lin, K. D. Chang, Y. C. Yu, J. T. W. Wang, C. S. Chang, L. J. Li, and T. W. Lin, "Synthesis of Large-Area MoS<sub>2</sub> Atomic Layers with Chemical Vapor Deposition" *Adv. Mater.* **24**, 2320-2325 (2012).

- [165] S. Najmaei, Z. Liu, W. Zhou, X. Zou, G. Shi, S. Lei, B. I. Yakobson, J. C. Idrobo, P. M. Ajayan, and J. Lou, "Vapour Phase Growth and Grain Boundary Structure of Molybdenum Disulphide Atomic Layers" *Nat. Mater.* **12**, 754-759 (2013).
- [166] B. Liu, M. Fathi, L. Chen, A. Abbas, Y. Ma, and C. Zhou, "Chemical Vapor Deposition Growth of Monolayer WSe<sub>2</sub> with Tunable Device Characteristics and Growth Mechanism Study" *ACS Nano* **9**, 6119-6127 (2015).
- [167] J. C. Shaw, H. Zhou, Y. Chen, N. O. Weiss, Y. Liu, Y. Huang, and X. Duan, "Chemical Vapor Deposition Growth of Monolayer MoSe<sub>2</sub> Nanosheets" *Nano Res.* **7**, 511-517 (2014).
- [168] Y. Yoon, K. Ganapathi and S. Salahuddin, "How Good Can Monolayer MoS<sub>2</sub> Transistors Be?" *Nano Lett.* **11**, 3768-3773 (2011).
- [169] H. Wang, L. Yu, Y. H. Lee, Y. Shi, A. Hsu, M. L. Chin, L. J. Li, M. Dubey, J. Kong, and T. Palacios, "Integrated Circuits Based on Bilayer MoS<sub>2</sub> Transistors" *Nano Lett.* **12**, 4674-4680 (2012).
- [170] Y. J. Zhang, J. T. Ye, Y. Matsushashi and Y. Iwasa, "Ambipolar MoS<sub>2</sub> Thin Flake Transistors" *Nano Lett.* **12**, 1136 (2012).
- [171] Q. H. Wang, K. Kalantar-Zadeh, A. Kis, J. N. Coleman and M. S. Strano, "Electronics and optoelectronics of two-dimensional transition metal dichalcogenides" *Nature Nanotech.* **7**, 699-712 (2012).

- [172] D. Xiao, G. B. Liu, W. Feng, X. Xu, and W. Yao, "Coupled spin and valley physics in monolayers of MoS<sub>2</sub> and other group-VI dichalcogenides" *Phys. Rev. Lett.* **108**, 196802 (2012).
- [173] W. Yao, D. Xiao, and Q. Niu, "Valley-dependent optoelectronics from inversion symmetry breaking" *Phys. Rev. B* **77**, 235406 (2008).
- [174] A. Splendiani, L. Sun, Y. Zhang, T. Li, J. Kim, C. Y. Chim, G. Galli, and F. Wang, "Emerging Photoluminescence in Monolayer MoS<sub>2</sub>" *Nano Lett.* **10**, 1271 (2010).
- [175] J. S. Ross, S. Wu, H. Yu, N. Ghimire, A. Jones, G. Aivazian, J. Yan, D. Mandrus, D. Xiao, W. Yao, and X. Xu, "Electrical control of neutral and charged excitons in a monolayer semiconductor" *Nat. Commun.* **4**, 1474 (2013).
- [176] T. Cao, G. Wang, W. Han, H. Ye, C. Zhu, J. Shi, Q. Niu, P. Tan, E. Wang, B. Liu, and J. Feng, "Valley-selective circular dichroism of monolayer molybdenum disulphide" *Nat. Commun.* **3**, 887 (2012).
- [177] M. Inoue, "Landau Levels and Cyclotron Resonance in Graphite", *J. Phys. Soc. Jap* **17**, 808 (1962).
- [178] T. Morimoto, and M. Koshino, "Gate-induced Dirac cones in multilayer graphenes", *Phys. Rev. B* **87**, 085424 (2013).
- [179] S. J. Tsai, Y. H. Chiu, Y. H. Ho, M. F. Lin, "Gate-voltage-dependent Landau levels in AA-stacked bilayer graphene" *Chem. Phys. Lett.* **550**, 104-110 (2012)
- [180] G. H. Li, A. Luican, and E. Y. Andrei, "Scanning Tunneling Spectroscopy of Graphene on Graphite" *Phys. Rev. Lett.* **102**, 176804 (2009).

- [181] D. L. Miller, K. D. Kubista, G. M. Rutter, M. Ruan, W. A. de Heer, P. N. First, and J. A. Stroscio, "Observing the Quantization of Zero Mass Carriers in Graphene" *SCIENCE* **324**, 924 (2009).
- [182] A. Luican, G. H. Li, A. Reina, J. Kong, R. R. Nair, K. S. Novoselov, A. K. Geim, and E. Y. Andrei, "Single-Layer Behavior and Its Breakdown in Twisted Graphene Layers" *Phys. Rev. Lett.* **106**, 126802 (2011).
- [183] Y. J. Song, A. F. Otte, Y. Kuk, Y. K. Hu, D. B. Torrance, P. N. First, W. A. de Heer, H. K. Min, S. Adam, M. D. Stiles, A. H. MacDonald, and J. A. Stroscio, "High-Resolution Tunnelling Spectroscopy of a Graphene Quartet" *Nature* **467**, 185 (2010).
- [184] W. X. Wang, L. J. Yin, J. B. Qiao, T. Cai, S. Y. Li, R. F. Dou, J. C. Nie, X. S. Wu, and L. He, "Atomic Resolution Imaging of the Two-Component Dirac-Landau Levels in a Gapped Graphene Monolayer" *Phys. Rev. B* **92**, 165420 (2015).
- [185] Z. Y. Zhu, Y. C. Cheng, and U. Schwingenschlögl, "Giant spin-orbit-induced spin splitting in two-dimensional transition-metal dichalcogenide semiconductors", *Phys. Rev. B* **84**, 153402 (2011).
- [186] S. Lebègue and O. Eriksson, "Electronic structure of two-dimensional crystals from ab initio theory", *Phys. Rev. B* **79**, 11409 (2009).
- [187] C. Ataca and S. Ciraci, "Functionalization of Single-Layer MoS<sub>2</sub> Honeycomb Structures", *J. Phys. Chem. C* **115**, 13303 (2011).

- [188] G. B. Liu W.-Y. Shan, Y. Yao, W. Yao, and D. Xiao, "Three-band tight-binding model for monolayers of group-VIB transition metal dichalcogenides", *Phys. Rev. B* **88**, 085433 (2013).
- [189] G. M. Rutter, S. Jung, N. N. Klimov, D. B. Newell, N. B. Zhitenev, J. A. Stroscio, "Microscopic polarization in bilayer graphene", *Nat. Phys.* **7**, 649 (2011).
- [190] L. J. Yin, Y. Zhang, J. B. Qiao, S. Y. Li, and L. He, "Experimental observation of surface states and Landau levels bending in bilayer graphene", *Phys. Rev. B* **93**, 125422 (2016).
- [191] L. J. Yin, S. Y. Li, J. B. Qiao, J. C. Nie, and L. He, "Landau quantization in graphene monolayer, Bernal bilayer, and Bernal trilayer on graphite surface", *Phys. Rev. B* **91**, 115405 (2015).
- [192] G. H. Li, and E. Y. Andrei, "Observation of Landau levels of Dirac fermions in graphite", *Nat. Phys.* **3**, 623 (2007).
- [193] S. Y. Zhou, G. H. Gweon, J. Graf, A. V. Fedorov, C. D. Spataru, R. D. Diehl, Y. Kopelevich, D. H. Lee, S. G. Louie, and A. Lanzara, "First direct observation of Dirac fermions in graphite", *Nat. Phys.* **2**, 595 (2006).
- [194] T. Matsui, H. Kambara, Y. Niimi, K. Tagami, M. Tsukada, and Hiroshi Fukuyama, "STS Observations of Landau Levels at Graphite Surfaces", *Phys. Rev. Lett.* **94**, 226403 (2005).

- [195] M. Orlita, C. Faugeras, J. M. Schneider, G. Martinez, D. K. Maude, and M. Potemski, "Graphite from the Viewpoint of Landau Level Spectroscopy: An Effective Graphene Bilayer and Monolayer", *Phys. Rev. Lett.* **102**, 166401 (2009).
- [196] C. H. Ho, S. J. Tsai, R. B. Chen, Y. H. Chiu, and M. F. Lin, "Low-energy Landau level spectrum in ABC-stacked trilayer graphene", *J. Nanosci. Nanotechnol.* **11**, 4938 (2011).
- [197] C. H. Ho, C. P. Chang, W. P. Su and M. F. Lin, "Precessing anisotropic Dirac cone and Landau subbands along a nodal spiral", *New J. Phys.* **15**, 053032 (2013).
- [198] H. Ajiki, and T. Ando, "Energy Bands of Carbon Nanotubes in Magnetic Fields", *J Phys. Soc. Jpn.* **65**, 505 (1995). (1996).

## Figure Captions

Figure 1: (a) Geometric structure of honeycomb graphene with an enlarged rectangular unit cell in  $B_z \hat{z}$ , and (b) the buckled (silicene, germanene, tinene) with (c) the  $sp^3$  bondings.

Figure 2: For monolayer graphene at  $B_z=40$  T, (a) the low-lying valence and conduction LLs, and the probability distributions of the subenvelope functions at the (b) A and (B) sublattices. The unit of the x-axis is  $2R_B$ , in which  $i$  represents the  $i$ -th A or B atom in an enlarged unit cell.

Figure 3: (a) Geometric structure and (b) energy bands of the ABC-stacked tetralayer graphene.  $\gamma_i$ 's denote the intralayer and interlayer hopping integrals.

Figure 4: The  $B_z$ -dependent LL energy spectrum of the ABC-stacked tetralayer graphene for (a) the first group, (b) the other three groups; (c) the four LLs nearest to  $E_F$ .

Figure 5: (a) The intragroup and intergroup LL anticrossing phenomena in the ABC-stacked tetralayer graphene. The spatial evolutions of subenvelope functions are shown in (b)–(i) for the second group of LLs, and (j)–(q) for the second and the third groups of LLs.

Figure 6: (a) Geometric structure of sliding bilayer graphene along the armchair direction; (b) energy bands and (c)  $B_z$ -dependent LL spectrum at  $\delta=6b/8$ .

Figure 7: (a) Energy bands of monolayer germanene and silicene, and (b)&(c) orbital-decomposed state probabilities along the high-symmetry points. The inset of (a) is the band structure near the Dirac point.

Figure 8: For germanene at  $B_z=15$  T, (a) & (b) the up-dominated and (c) & (d) the down-dominated LL energies and spatial probability distributions, corresponding to the quantized  $K$ -valley states.



Figure 9: (a) The  $V_z$ -dependent LL energy spectra of germanene at  $B_z=15$  T, and (b) the LL crossing and anticrossing within a certain range of  $E^v$ . (c) and (d) the drastic changes of probability distributions during the LL anticrossings. The inset of (a) is the band structure at  $B_z=0$  and a critical  $V_z$ . The LL anticrossings are indicated by the red circles.

Figure 10: (a)-(c) Similar plot as Fig. 7, but shown for monolayer tinene. Also plotted in (b) are those from the quantized  $\Gamma$ -valley states.

Figure 11: (a) The  $B_z$ -dependent energy spectra of the first and second groups (black and blue curves) in tinene, and (b) density of states at  $B_z = 30$  T.

Figure 12: The  $V_z$ -dependent LL energy spectra at  $B_z=15$  T for (a) tinene and (b) silicene.

Figure 13: (a) The geometric structure and the first Brillouin zone of monolayer phosphorene, and (b) the AB stacking structure of bilayer phosphorene. Also, the intralayer and interlayer hopping integrals are marked in (a) and (b), respectively.

Figure 14: Energy bands of (a) monolayer and (b) bilayer phosphorene.

Figure 15: (a) The LL energies of bilayer phosphorene at  $B_z=30$  T and (b) the probability distributions. Also shown in (c) are the amplitudes of  $n^c = 1$  of the upper (solid curve) and lower (dashed curve) layers.

Figure 16: For monolayer and bilayer phosphorene, the  $n^c$ - and  $B_z$ -dependent LL energies are shown in (a) and (b) respectively. The black and purple dashed lines in (a) and (b) represent the linear dependence.

Figure 17: (a) Geometric structures for  $\text{MoS}_2$  monolayer with an enlarged rectangular unit cell in  $B_z\hat{z}$  and (b) the structure of trigonal prismatic coordination.

Figure 18. (a) Energy bands of monolayer MoS<sub>2</sub>, and (b)-(d) the orbital-decomposed state probabilities along the high-symmetry points.

Figure 19. (a) The  $B_z$ -dependent energy spectra of the valence LLs are, respectively, related to the quantized states near the  $(K, K')$  and  $\Gamma$  points (black and blue curves), in which the valley-dependent (spin-dependent) subgroups are represented by the solid and dashed curves (the red and yellow colors). The spatial probability distributions are shown in (b) at  $B_z=40$  T.

Fig. 20. Same plot as Fig. 19, but shown for the low-lying conduction LLs.

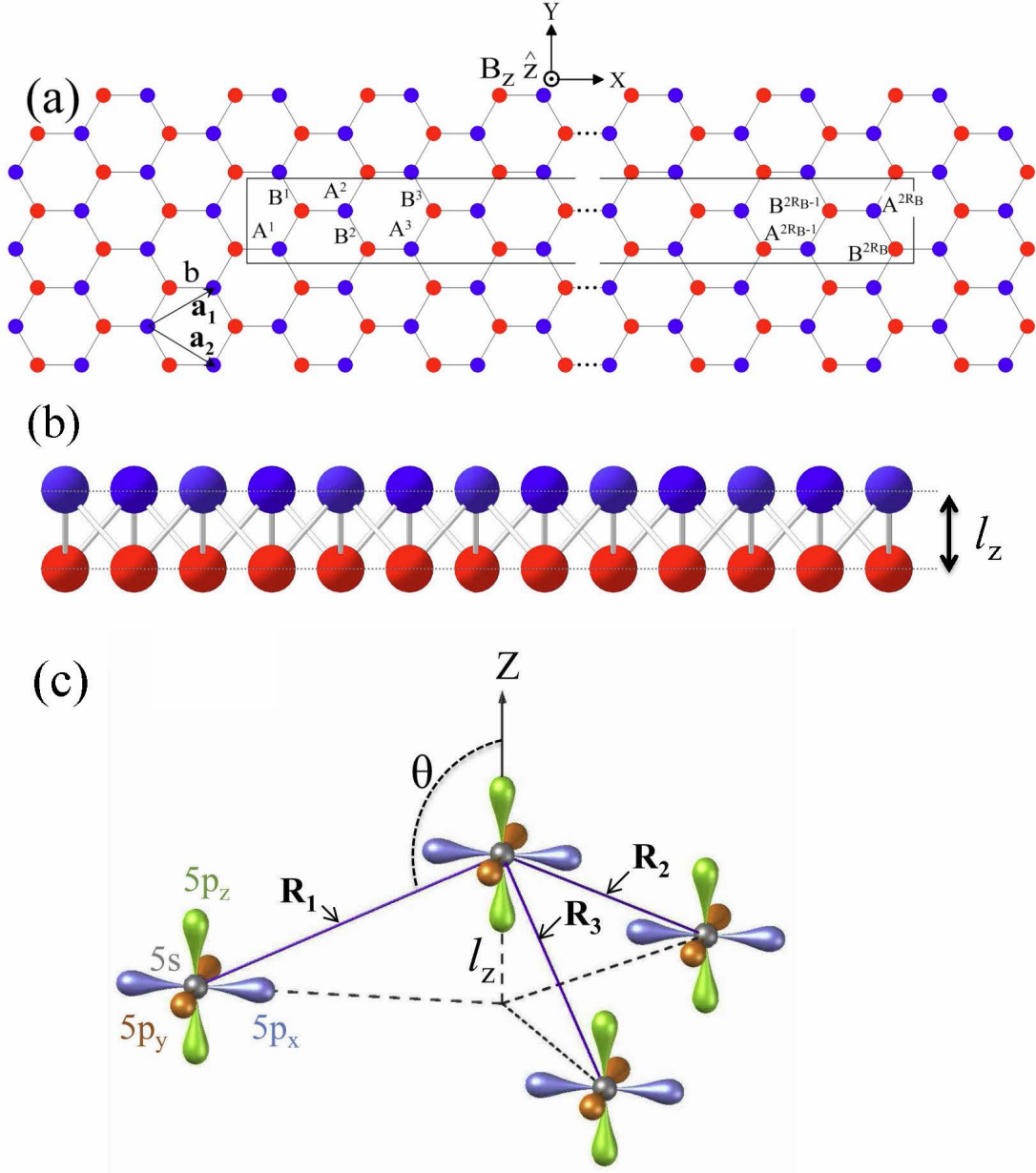


Figure 1: (a) Geometric structure of honeycomb graphene with an enlarged rectangular unit cell in  $B_z \hat{z}$ , and (b) the buckled (silicene, germanene, tinene) with (c) the  $sp^3$  bondings.

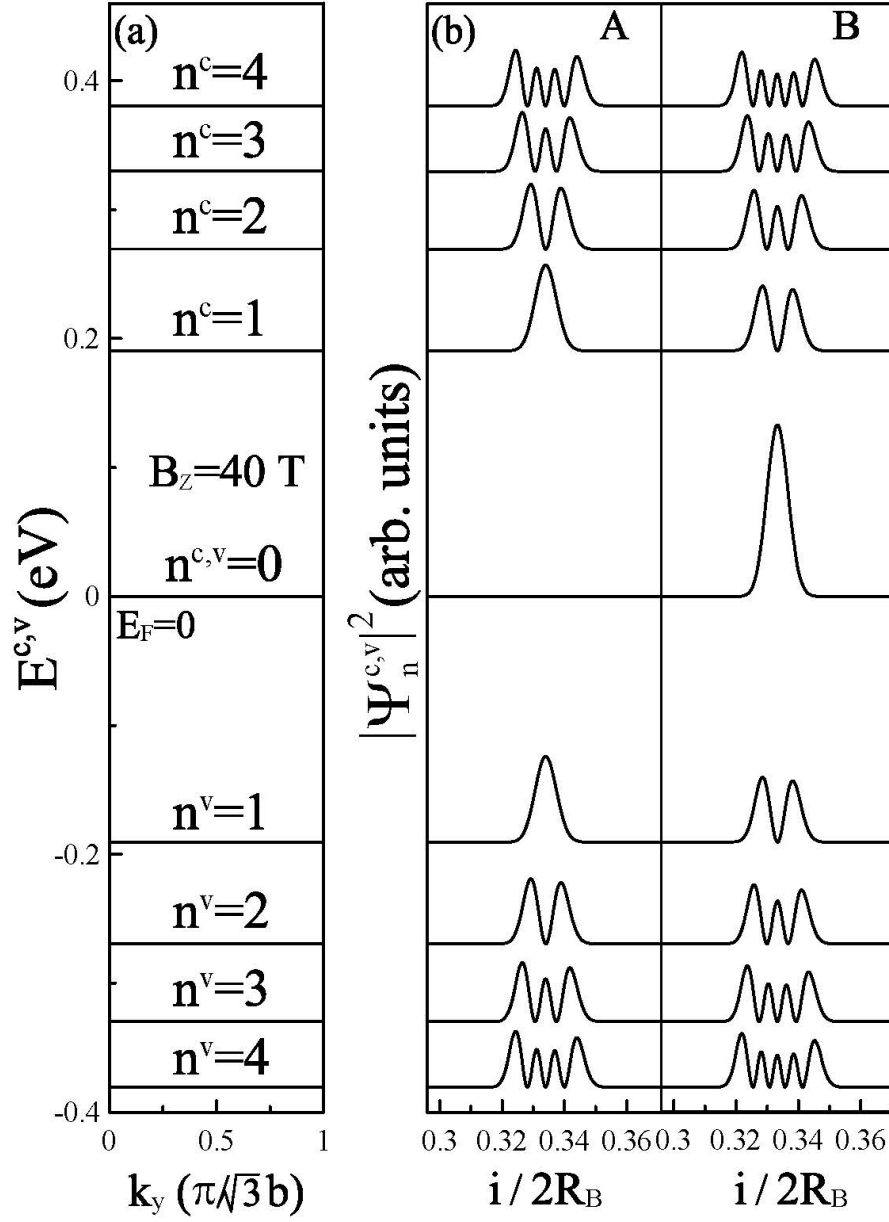


Figure 2: For monolayer graphene at  $B_z=40$  T, (a) the low-lying valence and conduction LLs, and the probability distributions of the subenvelope functions at the (b) A and (B) sublattices. The unit of the x-axis is  $2R_B$ , in which  $i$  represents the  $i$ -th A or B atom in an enlarged unit cell.

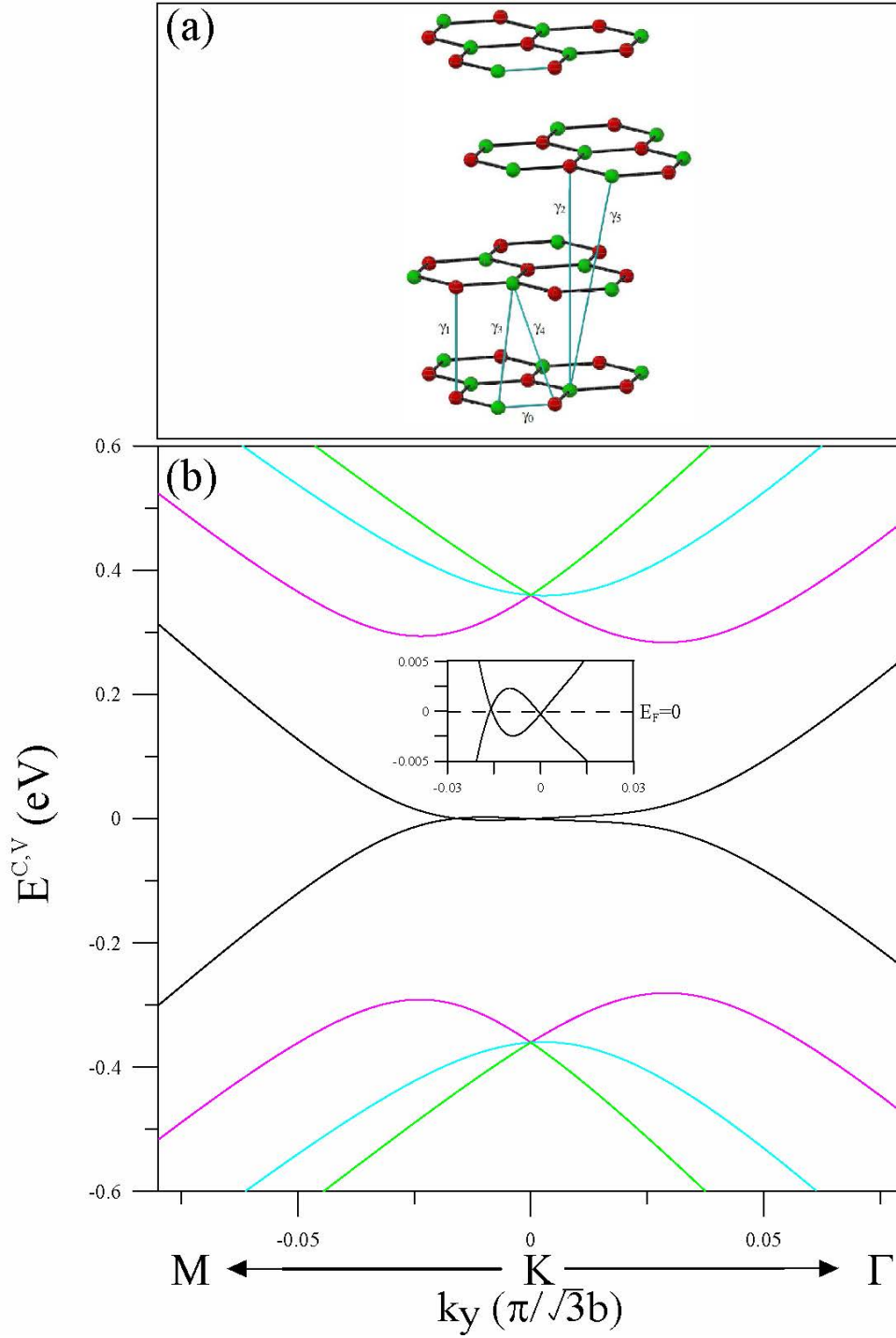


Figure 3: (a) Geometric structure and (b) energy bands of the ABC-stacked tetralayer graphene.  $\gamma_i$ 's denote the intralayer and interlayer hopping integrals.

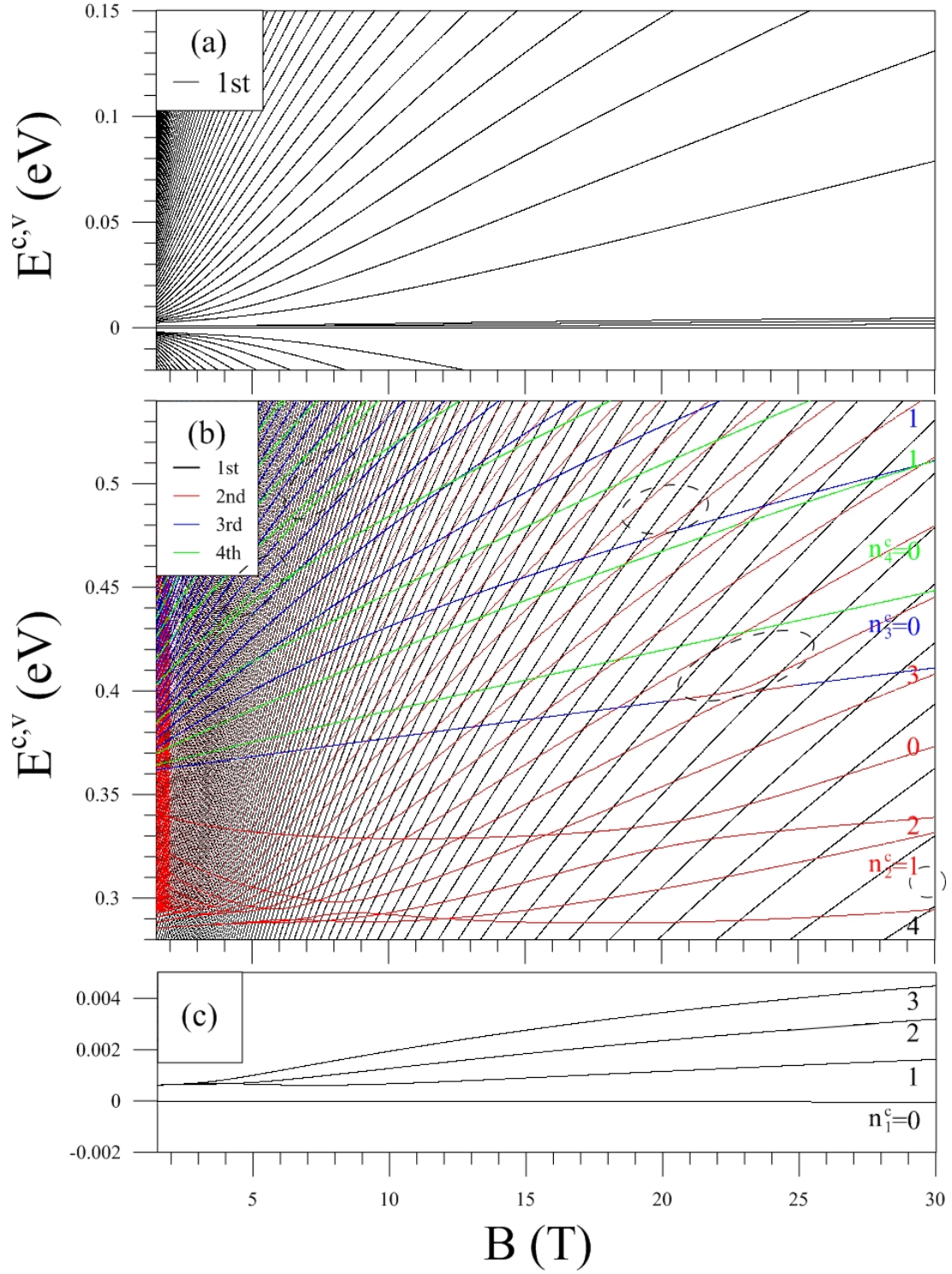


Figure 4: The  $B_z$ -dependent LL energy spectrum of the ABC-stacked tetralayer graphene for (a) the first group, (b) the other three groups; (c) the four LLs nearest to  $E_F$ .

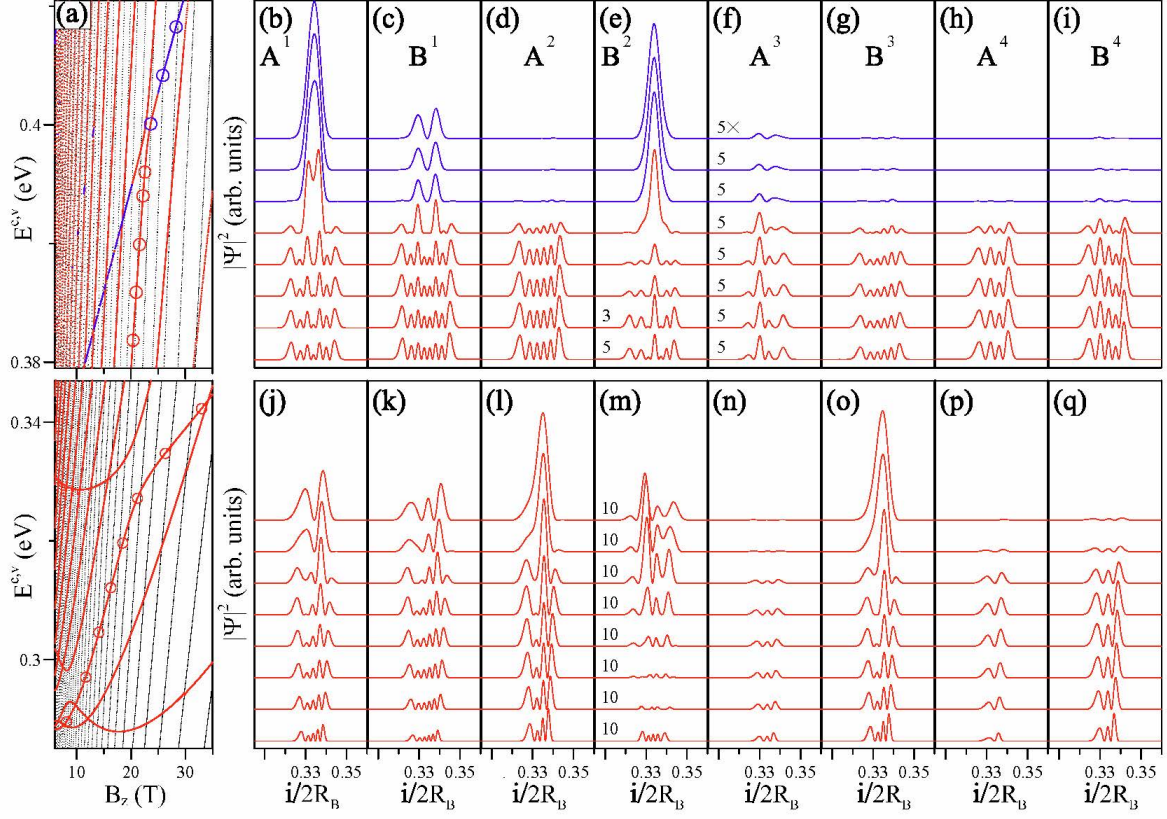


Figure 5: (a) The intragroup and intergroup LL anticrossing phenomena in the ABC-stacked tetralayer graphene. The spatial evolutions of subenvelope functions are shown in (b)-(i) for the second group of LLs, and (j)-(q) for the second and the third groups of LLs.



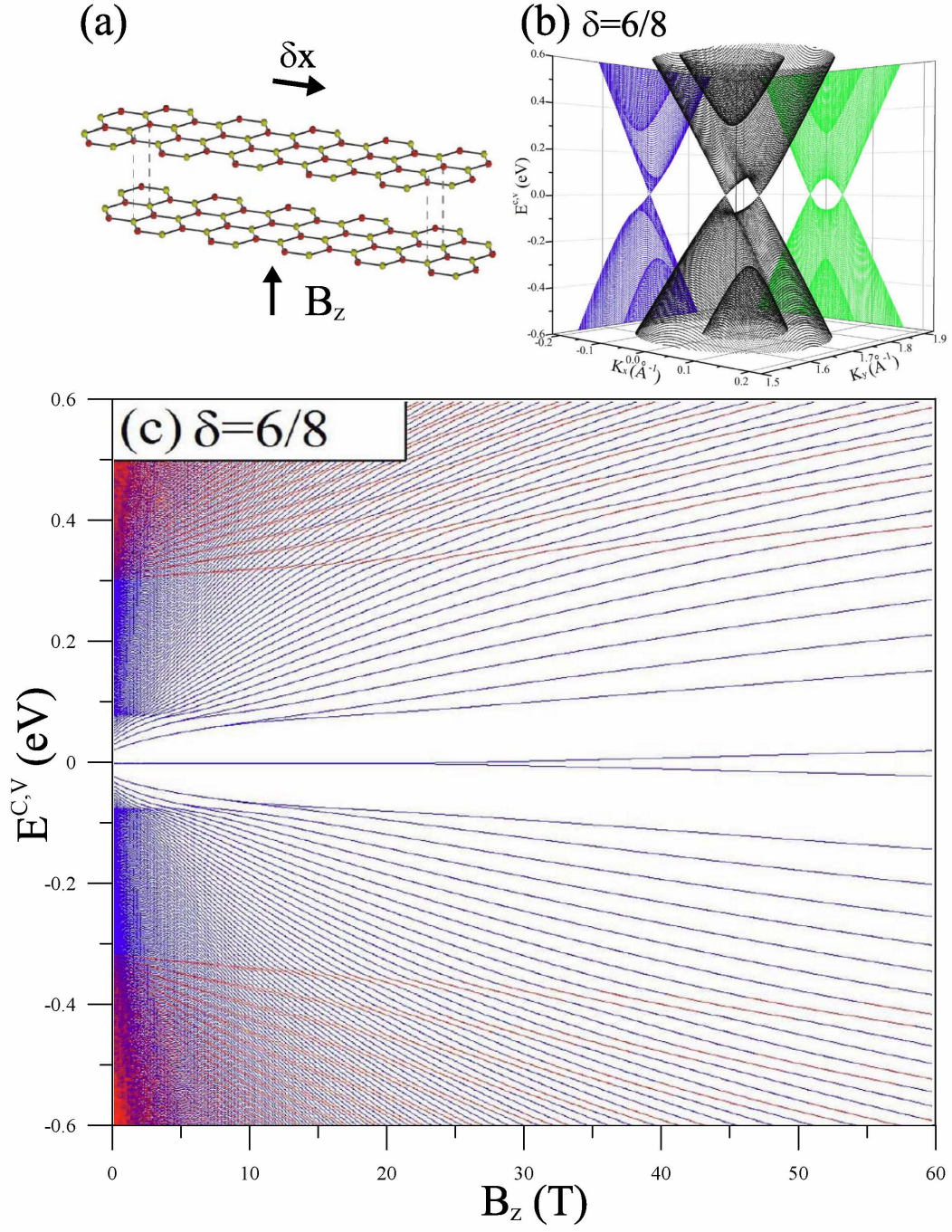


Figure 6: (a) Geometric structure of sliding bilayer graphene along the armchair direction; (b) energy bands and (c)  $B_z$ -dependent LL spectrum at  $\delta=6b/8$ .



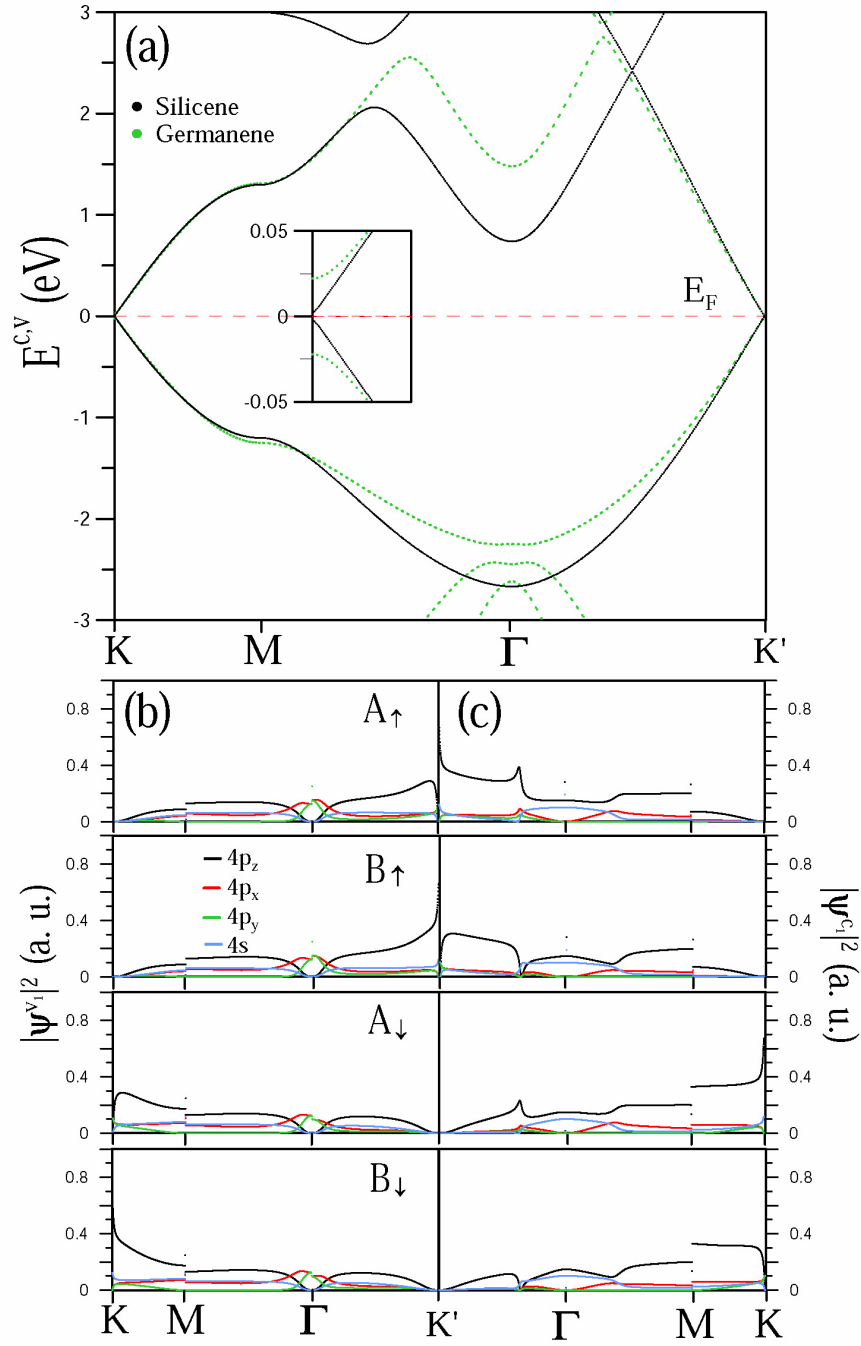


Figure 7: (a) Energy bands of monolayer germanene and silicene, and (b)&(c) orbital-decomposed state probabilities along the high-symmetry points. The inset of (a) is the band structure near the Dirac point.

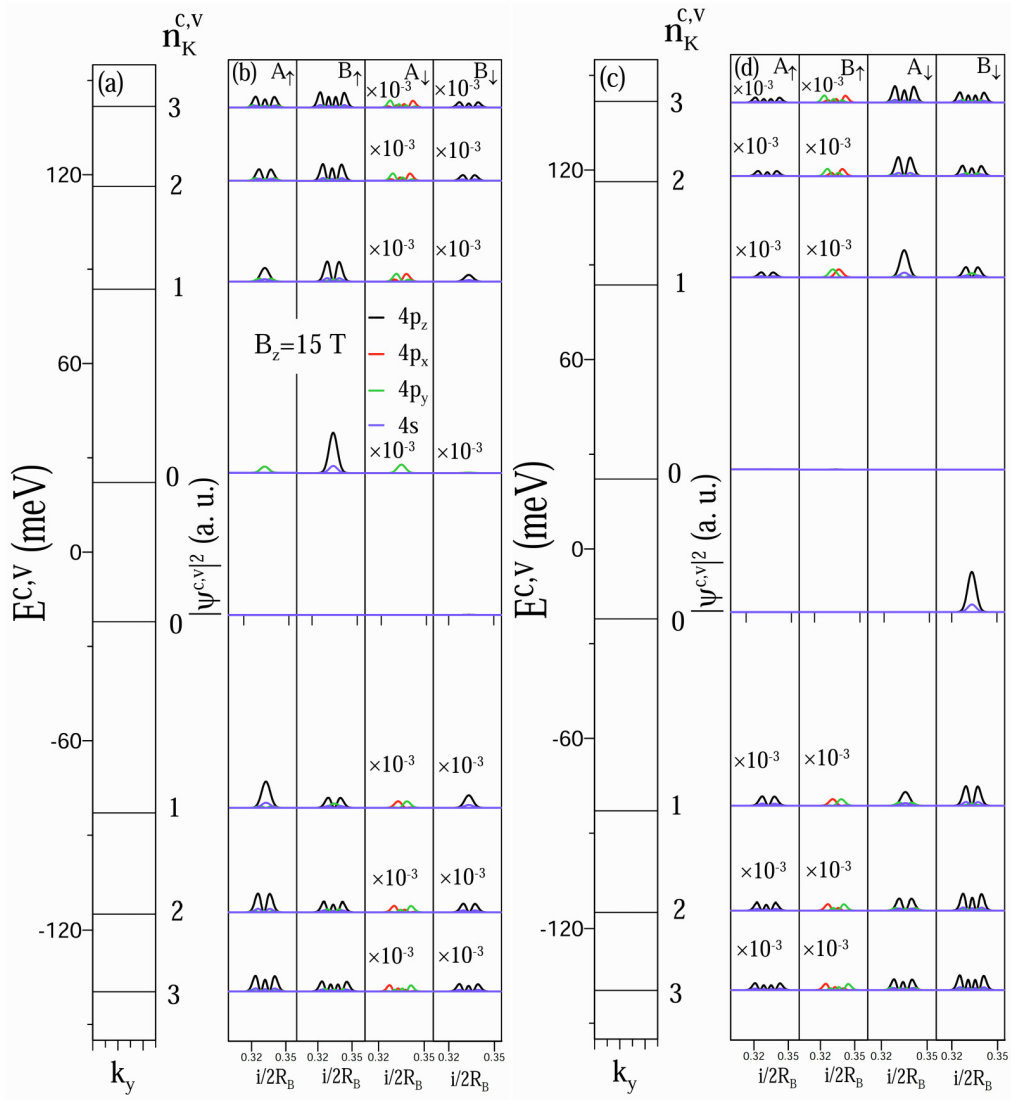


Figure 8: For germanene at  $B_z = 15$  T, (a) & (b) the up-dominated and (c) & (d) the down-dominated LL energies and spatial probability distributions, corresponding to the quantized  $K$ -valley states.

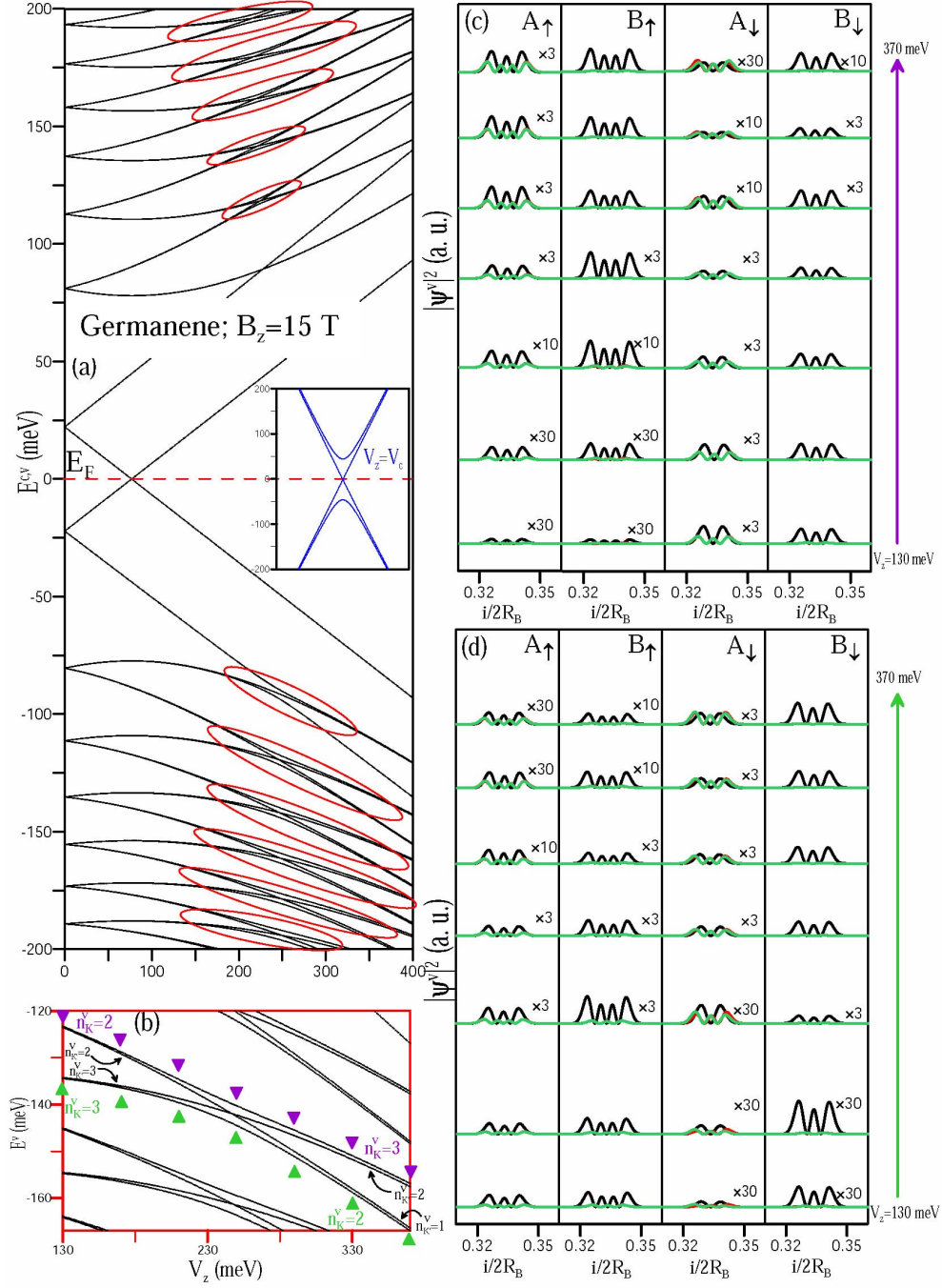


Figure 9: (a) The  $V_z$ -dependent LL energy spectra of germanene at  $B_z = 15$  T, and (b) the LL crossing and anticrossing within a certain range of  $E^v$ . (c) and (d) the drastic changes of probability distributions during the LL anticrossings. The inset of (a) is the band structure at  $B_z = 0$  and a critical  $V_z$ . The LL anticrossings are indicated by the red circles.

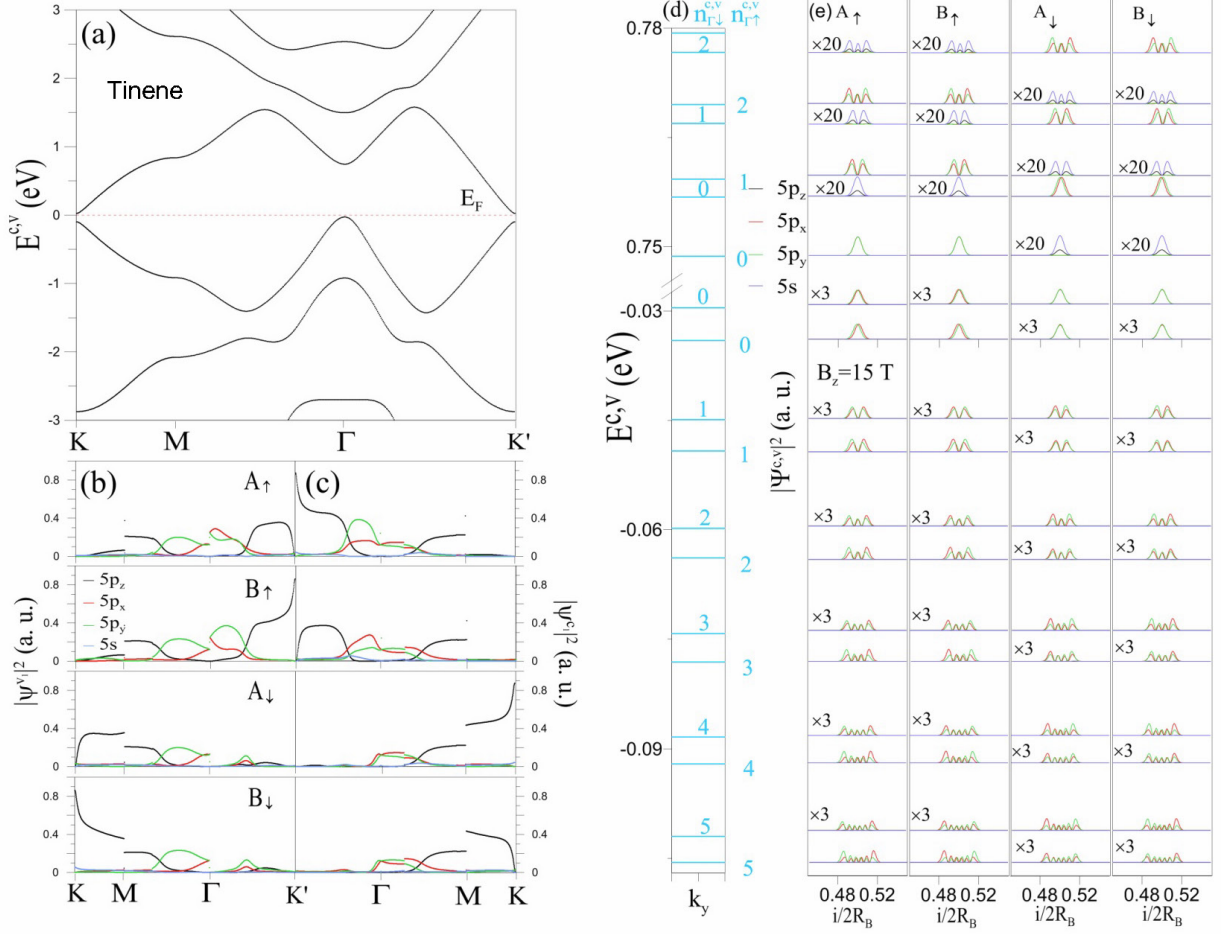


Figure 10: (a)-(c) Similar plot as Fig. 7, but shown for monolayer tinene. Also plotted in (b) are those from the quantized  $\Gamma$ -valley states.

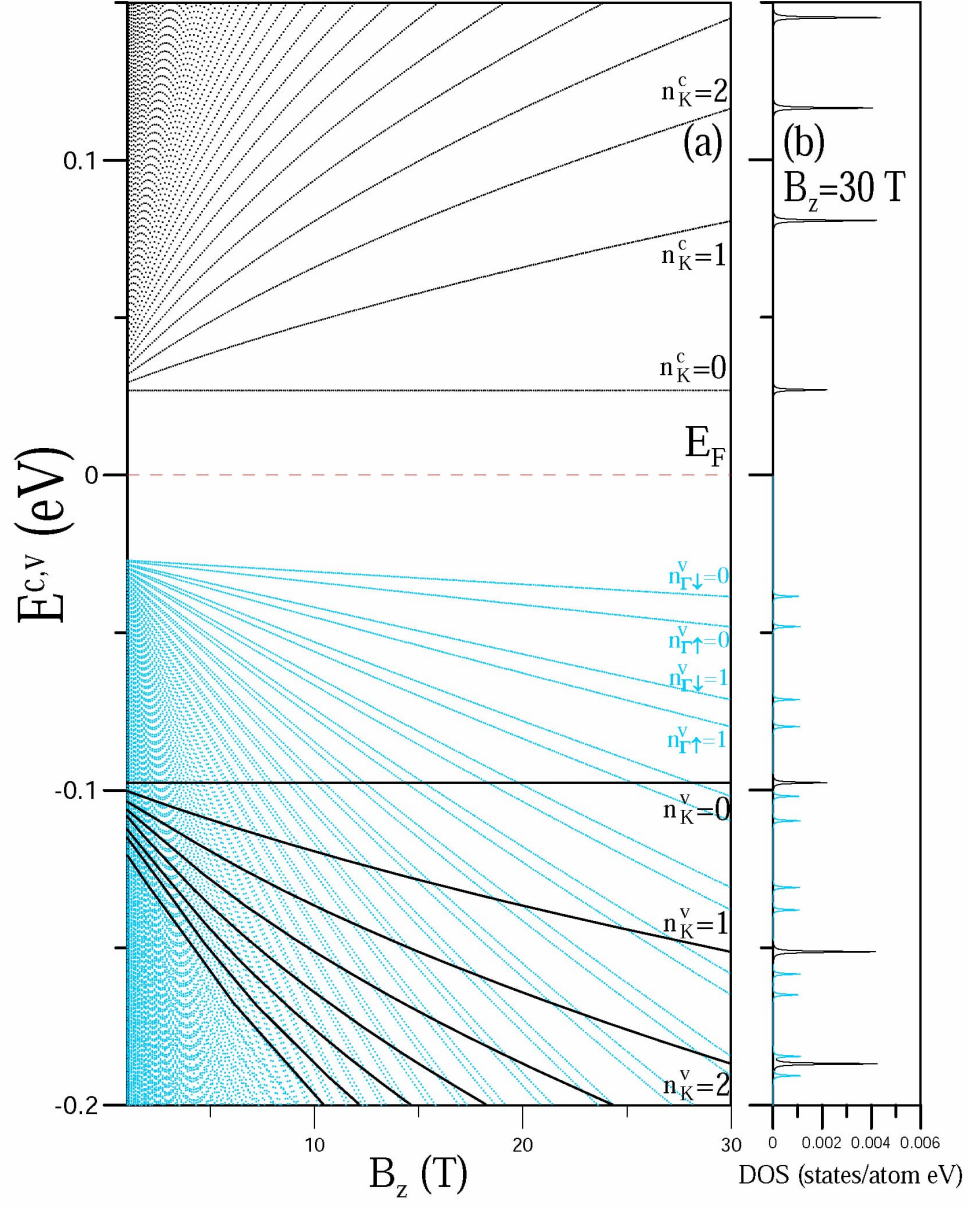


Figure 11: (a) The  $B_z$ -dependent energy spectra of the first and second groups (black and blue curves) in tinene, and (b) density of states at  $B_z = 30$  T.

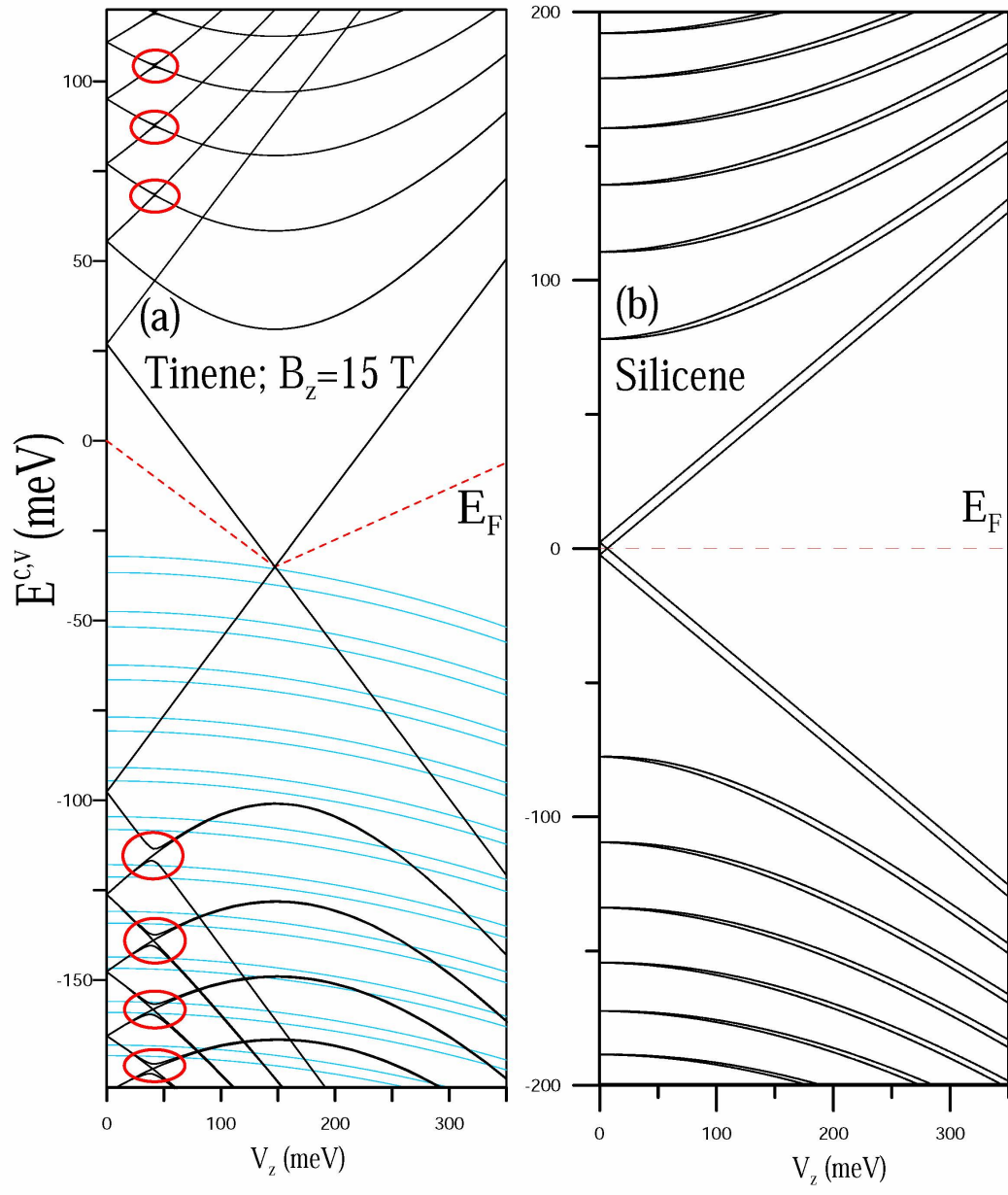


Figure 12: The  $V_z$ -dependent LL energy spectra at  $B_z = 15$  T for (a) tinene and (b) silicene.

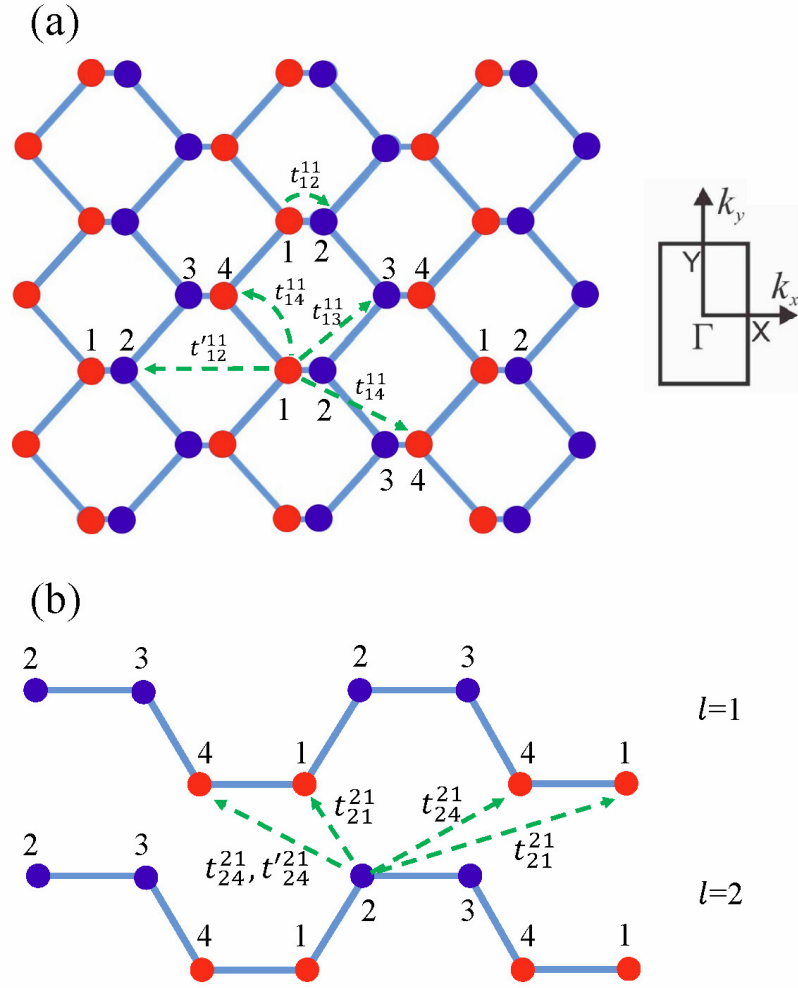


Figure 13: (a) The geometric structure and the first Brillouin zone of monolayer phosphorene, and (b) the AB stacking structure of bilayer phosphorene. Also, the intralayer and interlayer hopping integrals are marked in (a) and (b), respectively.

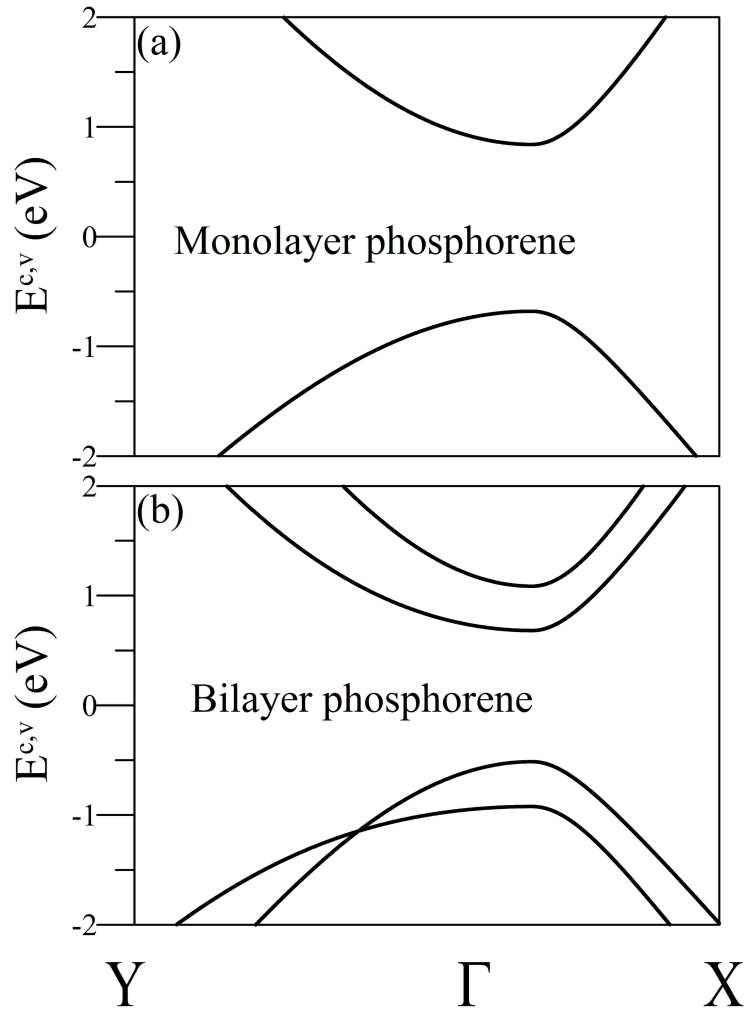


Figure 14: Energy bands of (a) monolayer and (b) bilayer phosphorene.



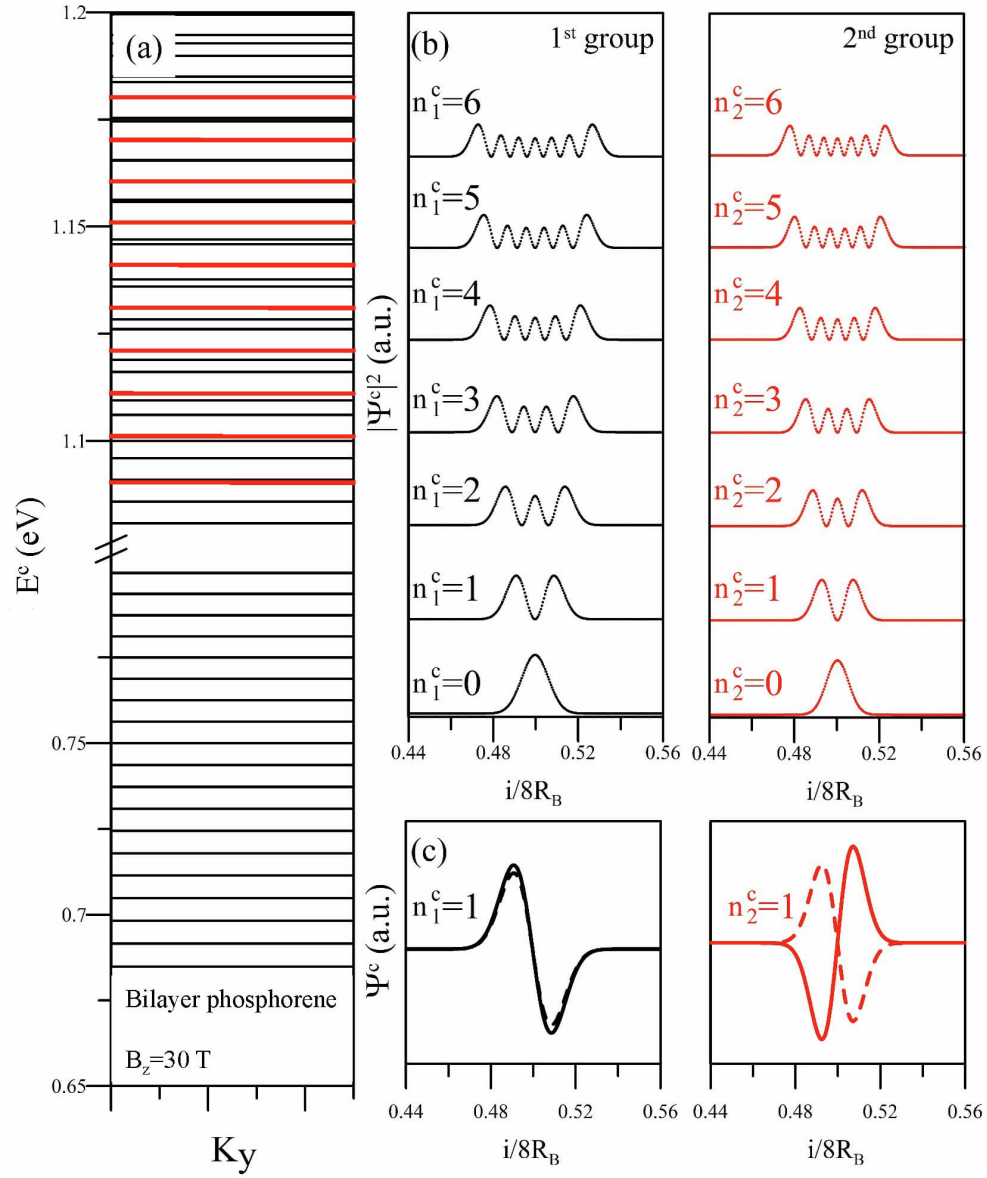


Figure 15: (a) The LL energies of bilayer phosphorene at  $B_z=30$  T and (b) the probability distributions. Also shown in (c) are the amplitudes of  $n^c = 1$  of the upper (solid curve) and lower (dashed curve) layers.

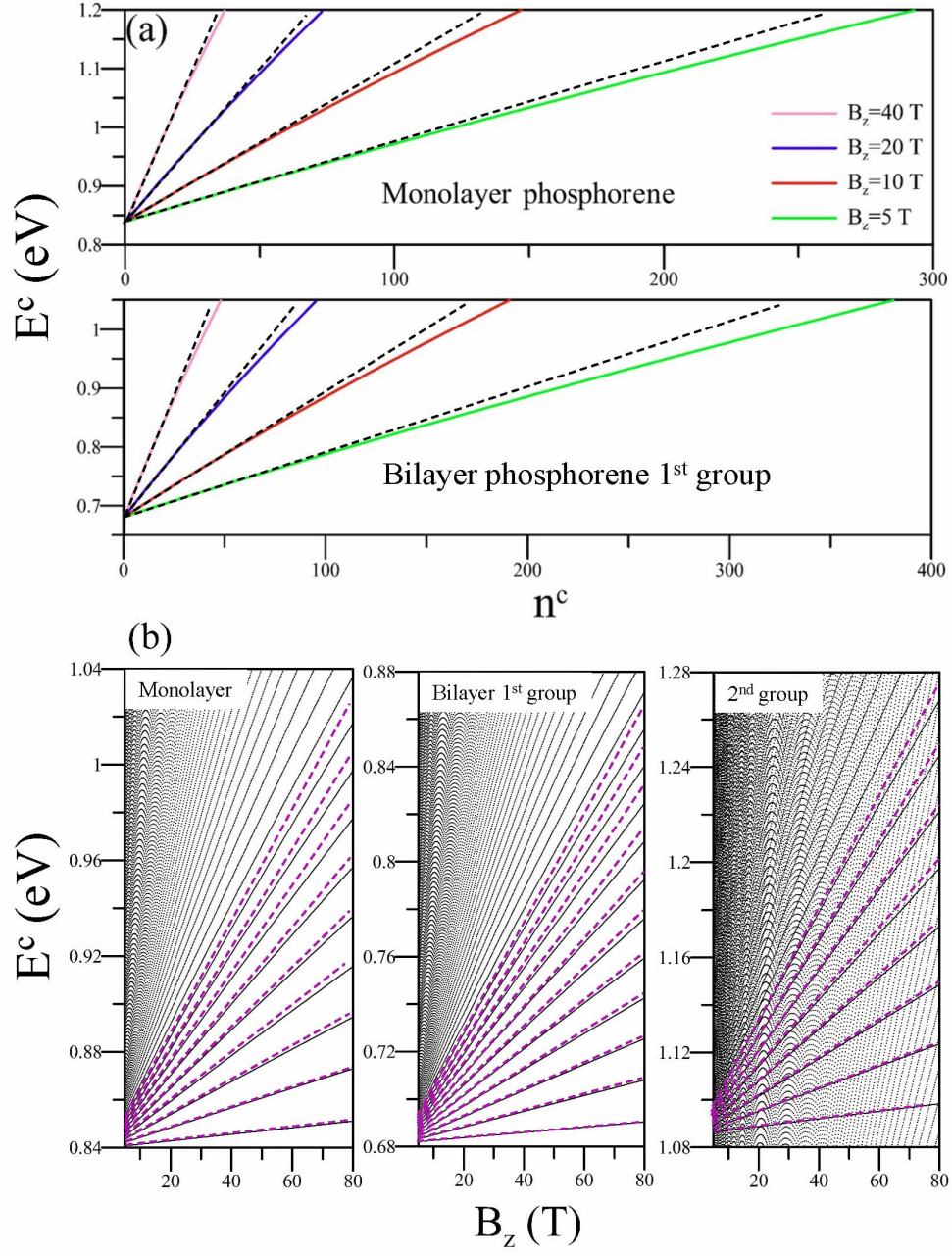


Figure 16: For monolayer and bilayer phosphorene, the  $n^c$ - and  $B_z$ -dependent LL energies are shown in (a) and (b) respectively. The black and purple dashed lines in (a) and (b) represent the linear dependence.

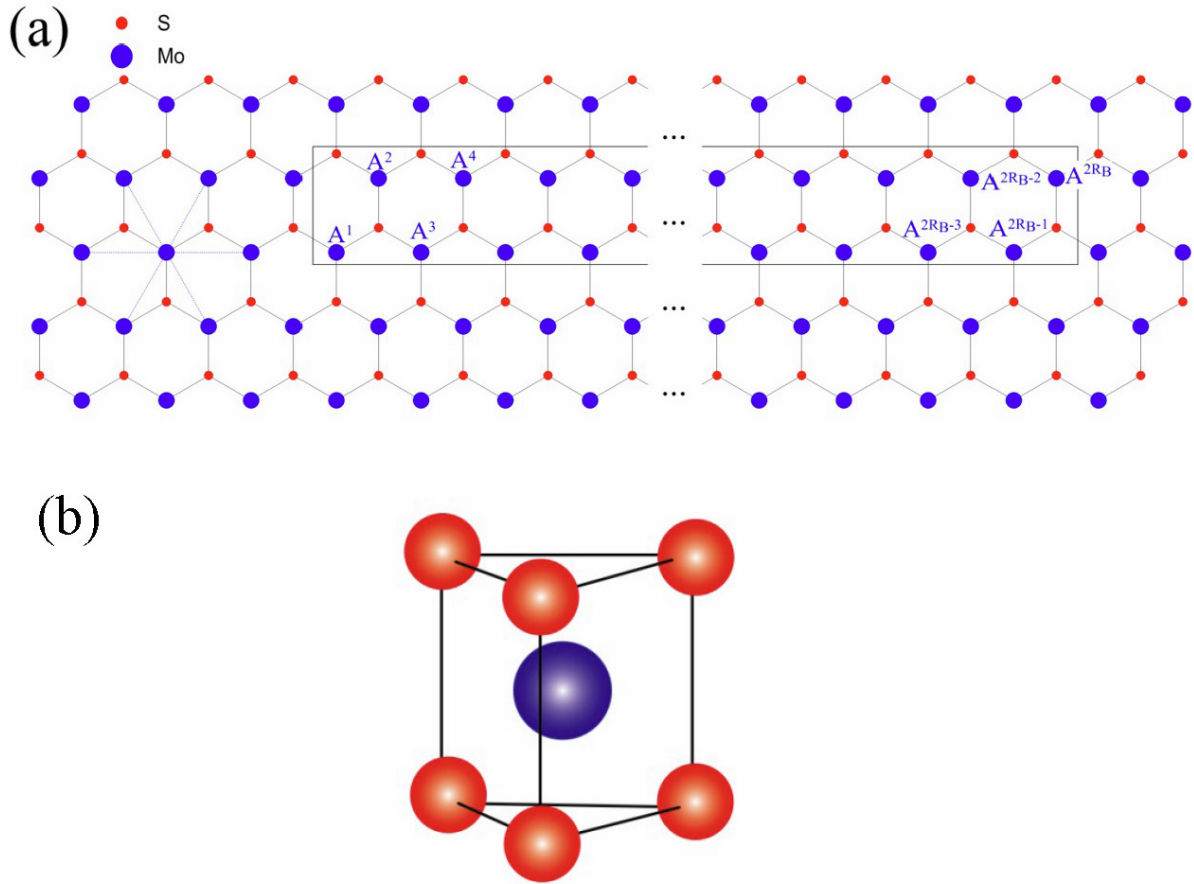


Figure 17: (a) Geometric structures for MoS<sub>2</sub> monolayer with an enlarged rectangular unit cell in  $B_z \hat{z}$  and (b) the structure of trigonal prismatic coordination.

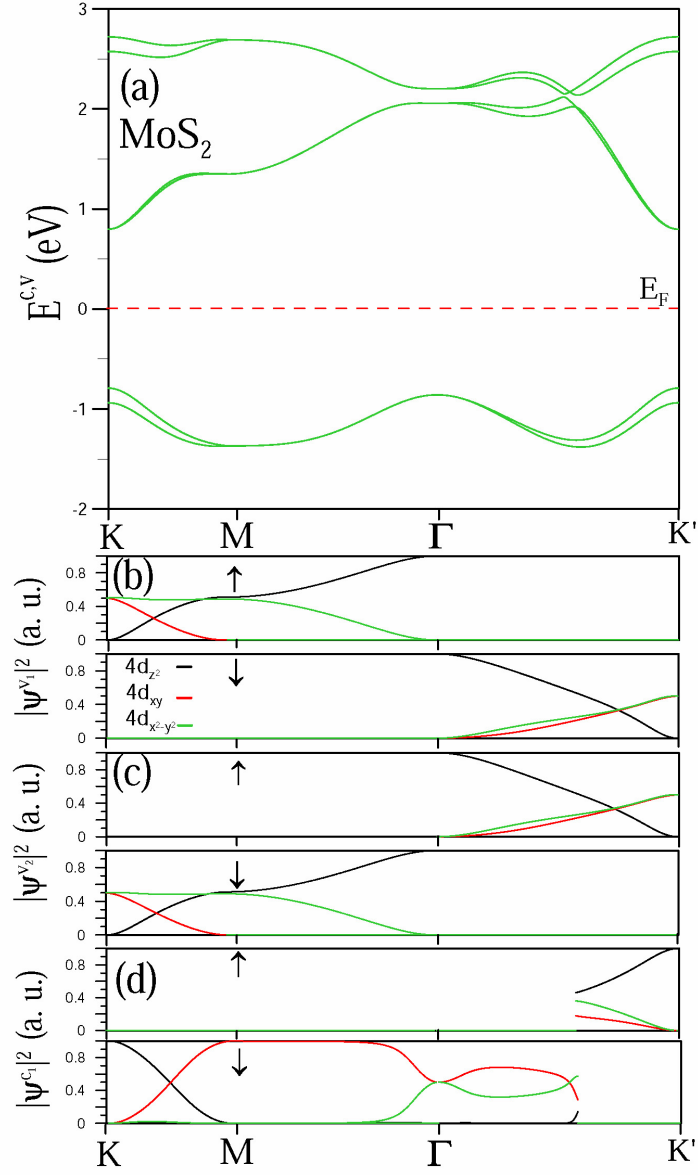


Figure 18: (a) Energy bands of monolayer MoS<sub>2</sub>, and (b)-(d) the orbital-decomposed state probabilities along the high-symmetry points.

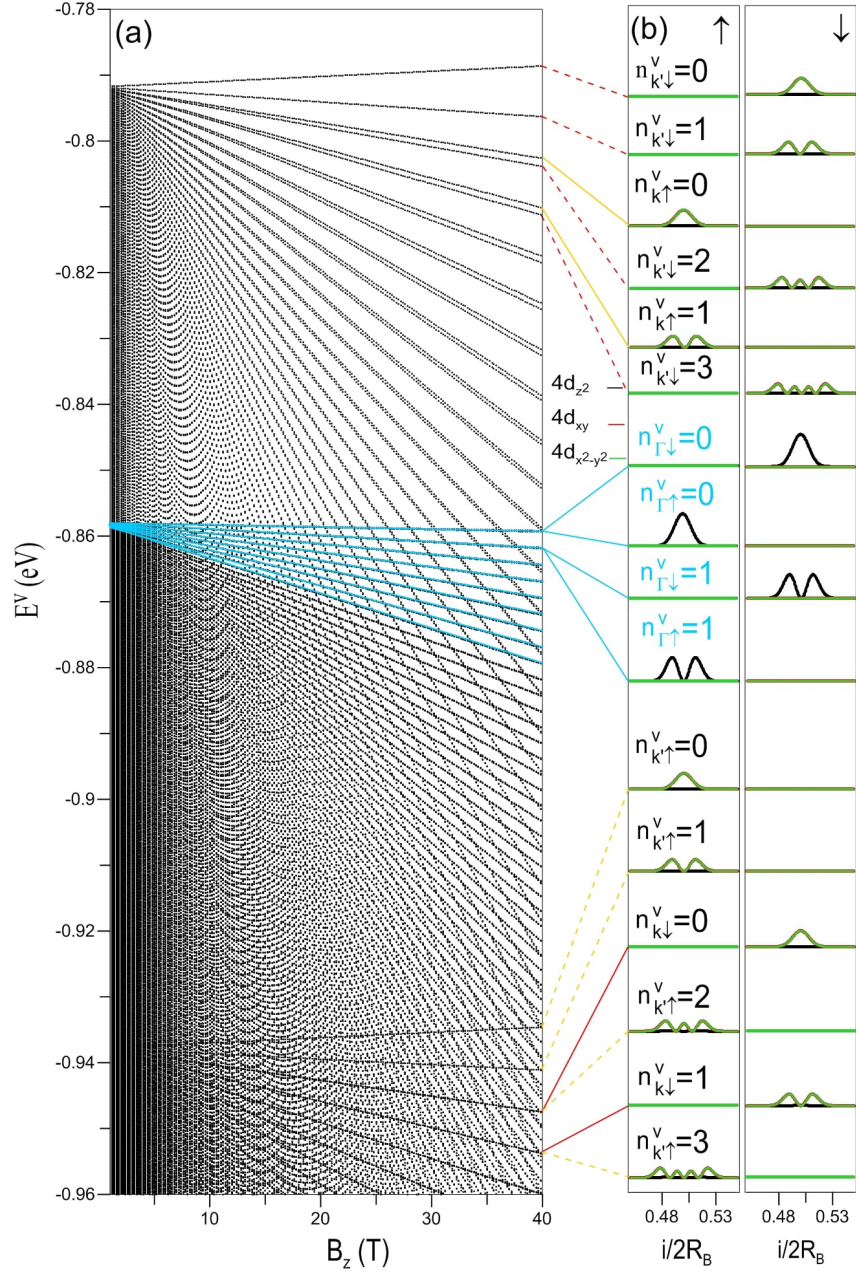


Figure 19: (a) The  $B_z$ -dependent energy spectra of the valence LLs are, respectively, related to the quantized states near the  $(K, K')$  and  $\Gamma$  points (black and blue curves), in which the valley-dependent (spin-dependent) subgroups are represented by the solid and dashed curves (the red and yellow colors). The spatial probability distributions are shown in (b) at  $B_z = 40$  T.



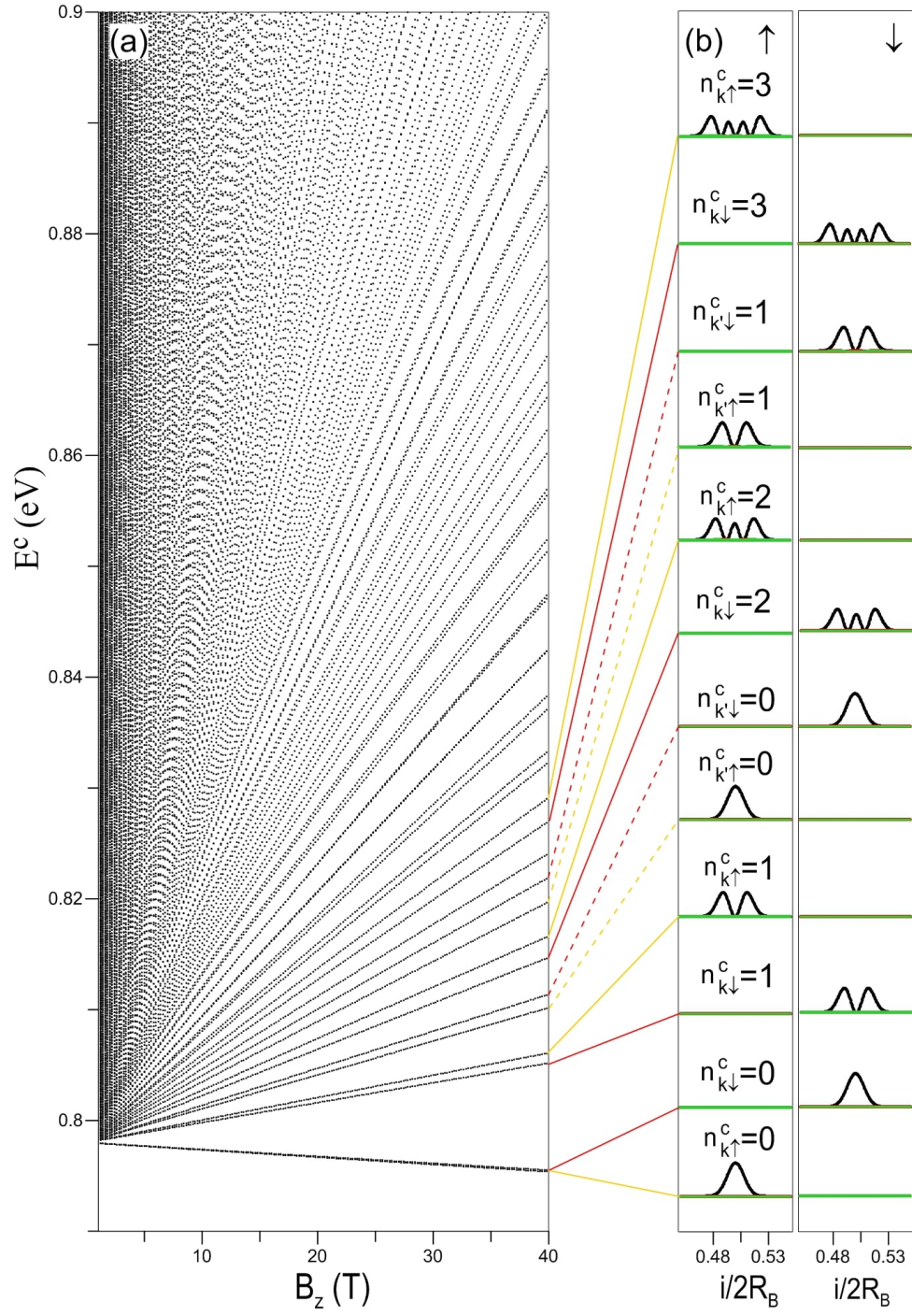


Figure 20: Same plot as Fig. 19, but shown for the low-lying conduction LLs.